JOURNAL OF GEOPHYSICAL RESEARCH, VOL. 114, A03215, doi:10.1029/2008JA013830, 2009

Goniopolarimetric study of the revolution 29 perikrone using the Cassini Radio and Plasma Wave Science instrument high-frequency radio receiver

B. Cecconi,[1] L. Lamy,[1] P. Zarka,[1] R. Prangé,[1] W. S. Kurth,[2] and P. Louarn[3]

Received 16 October 2008; revised 21 November 2008; accepted 10 December 2008; published 26 March 2009.

[1] We present goniopolarimetric (also known as direction finding) results of the Saturn kilometric radiation (SKR), using the Cassini Radio and Plasma Wave Science instrument high-frequency radio receiver data. Tools to retrieve the characteristics of the SKR sources have been developed that allow us to measure their 3-D location and beaming angle relative to the magnetic field in the source and, thus, to deduce the location of the footprints of the active magnetic field lines. We present results from these analyses on SKR observed during the revolution 29 perikrone (25–26 September 2006) with a relatively high orbital inclination. These results provide for the first time the observed beaming angle, the invariant latitude, and the local time of the SKR sources. We provide evidence that the SKR is mainly emitted in the right-hand extraordinary (R-X) mode and marginally in the left-hand ordinary (L-O) mode. We observe the footprint of the active magnetic field lines in the $\sim 70^\circ$ to $\sim 80^\circ$ northern and southern latitudinal range and in the 0400 to 1600 local time range. The northern sources are observed at slightly higher latitude than southern sources. The location matches that of the UV and IR aurorae. Duskside and nightside sources are also detected.

Citation: Cecconi, B., L. Lamy, P. Zarka, R. Prangé, W. S. Kurth, and P. Louarn (2009), Goniopolarimetric study of the revolution 29 perikrone using the Cassini Radio and Plasma Wave Science instrument high-frequency radio receiver, *J. Geophys. Res.*, *114*, A03215, doi:10.1029/2008JA013830.

1. Introduction

[2] Saturn's kilometric radiation (SKR) was discovered with the Voyager Planetary Radio Astronomy (PRA) experiment by *Kaiser et al.* [1980]. It is the most intense component of the kronian radio emissions (see reviews by *Kaiser et al.* [1984], *Zarka* [1998, 2000], and *Lamy et al.* [2008b]). This nonthermal radio emission covers the frequency range from 10 kHz to $\geq$1.2 MHz with a peak intensity at about 200 kHz. The SKR is sporadic and shows arc-like structures in the time-frequency space (see Figure 1a) [*Boischot et al.*, 1981; *Lamy et al.*, 2008a]. Various mechanisms for particle acceleration and auroral precipitation have been proposed [*Galopeau et al.*, 1995; *Cowley et al.*, 2004], and it is widely accepted that the SKR emission results from the cyclotron maser instability (CMI) [*Wu and Lee*, 1979; *Louarn*, 1992, and references therein]. In situ measurements within the emission region of the terrestrial auroral kilometric radiation (AKR) [*Ergun et al.*, 1998, 2000] proved the validity of this model in Earth's case. Even though no such in situ measurement has been carried out at other planets, this emission process is the one that best meets the observational constraints for nonthermal planetary radio emissions (such as polarization, brightness temperature, frequency cutoff, beaming and localization) [*Zarka*, 1998]. *Lamy et al.* [2008b] have shown that the SKR polarization characteristics are consistent with the CMI process: (1) the SKR is circularly polarized; (2) it is right-handed (RH) in the northern hemisphere and left-handed (LH) in the southern one, indicating an emission in the right-hand extraordinary (R-X) mode; and (3) the radio emission is strongly beamed. They also tentatively identified marginal ordinary (L-O) mode in dynamic spectra. Let us recall other characteristics of the CMI process: radio waves are emitted close to the local electron gyrofrequency (f_{ce}), along the walls of a hollow cone whose aperture (also known as the beaming angle) is large [*Queinnec and Zarka*, 1998; *Zarka*, 1998; *Hess et al.*, 2008; *Lamy et al.*, 2008a] and depends on the electron distribution function at the origin of the radio emission [*Wu*, 1985]. The visibility of the SKR is thus strongly dependent on the location of the observer, the location of the source and its beaming.

[3] The auroral origin of the SKR was inferred from the first observations [*Kaiser et al.*, 1980]. The SKR source locations have been indirectly deduced from the Voyager PRA data [*Galopeau et al.*, 1995, and references therein]: they were found to be quasi-fixed in local time (LT),

[1]LESIA, Observatoire de Paris, CNRS, UPMC, Université Paris Diderot, Meudon, France.
[2]Department of Physics and Astronomy, University of Iowa, Iowa City, Iowa, USA.
[3]Centre d'Etude Spatiale des Rayonnements, Université Paul Saltier, CNRS, Toulouse, France.

0148-0227/09/2008JA013830$09.00

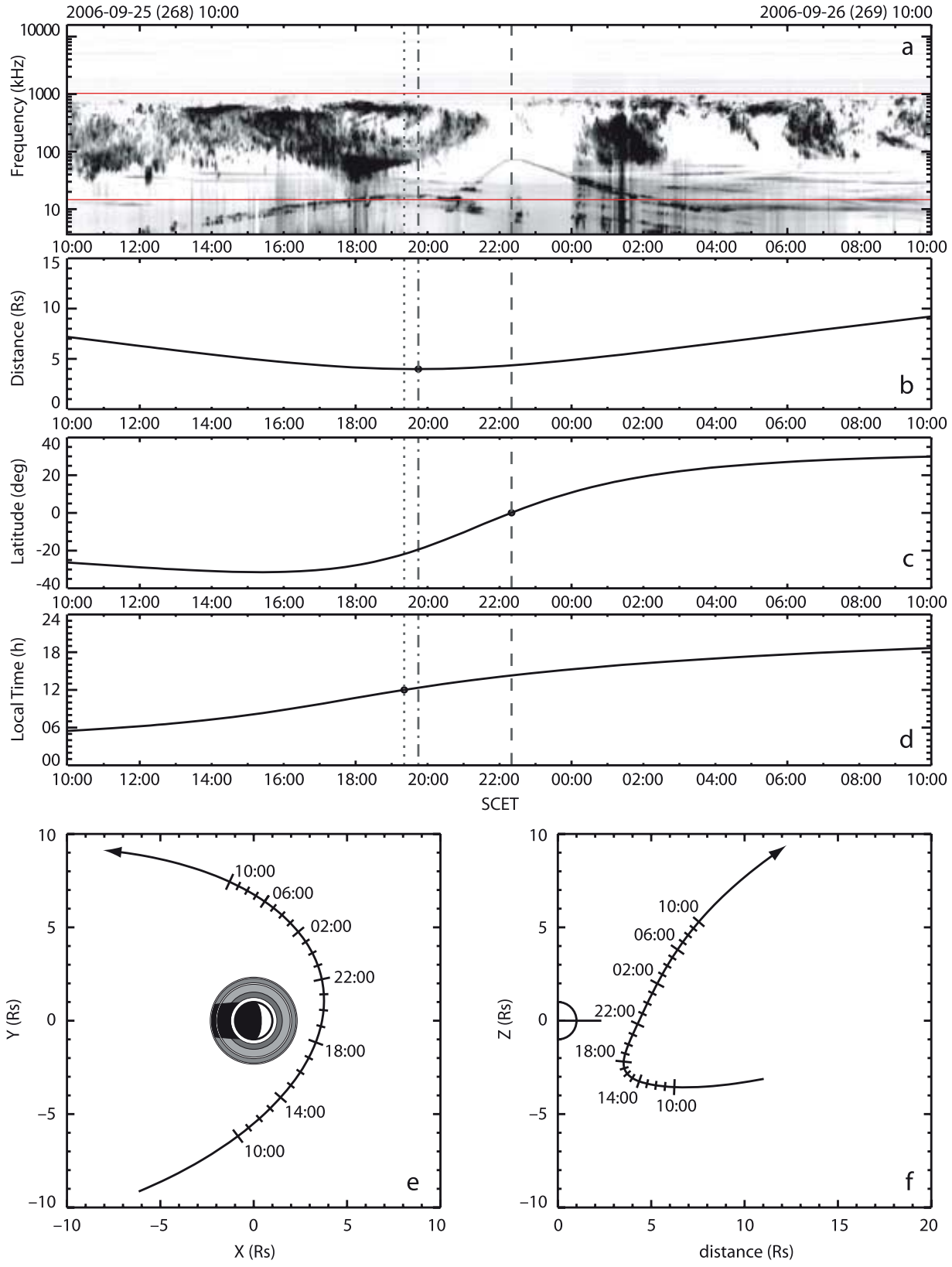
2006-09-25 (268) 10:00
2006-09-26 (269) 10:00
Frequency (kHz)
a
Distance (Rs)
b
Latitude (deg)
c
Local Time (h)
d
SCET
Y (Rs)
X (Rs)
e
Z (Rs)
distance (Rs)
f

Figure 1

centered approximately at noon (1200 LT), at high magnetic latitudes ($\geq 80°$), and extending toward lower latitudes on the morningside (down to 60° at ~0900 LT). This locus roughly matches the ultraviolet (UV) southern auroral oval of Saturn, observed from the Hubble Space Telescope (HST) [*Gérard et al.*, 1995; *Trauger et al.*, 1998; *Gérard et al.*, 2004; *Kurth et al.*, 2005; *Badman et al.*, 2006], as well as the infrared (IR) auroral oval [*Stallard et al.*, 2008a, 2008b].

[4] Launched in 1997, the Cassini spacecraft arrived at Saturn in July 2004. It is the fourth spacecraft (after Voyagers 1 and 2 and Ulysses) carrying radio astronomy instrumentation that can observe Saturn's radio emissions. The high-frequency receiver (HFR) of the Radio and Plasma Wave Science instrument (RPWS) experiment has goniopolarimetric (GP) capabilities (also referred to as direction finding in the literature) [*Gurnett et al.*, 2004]. This means that it is possible to retrieve the polarization (polarization Stokes parameters: U and Q for linear polarization, V for circular polarization), the direction of arrival (two angles defining the **k** vector: the colatitude θ and the azimuth ϕ) and the flux (S) of an incoming transverse electromagnetic wave. Moreover, the RPWS/HFR GP capabilities are quasi-instantaneous (10−80 ms) as compared to GP on spinning spacecraft like Ulysses or Wind for which at least one rotation of the spacecraft is needed to obtain GP measurements (12 s for Ulysses). The GP inversion we use in this paper is described by *Cecconi* [2004] and *Cecconi and Zarka* [2005].

[5] In this study, we present goniopolarimetric results for the perikrone of orbit revolution (Rev) 29. A description of the data and the applied preprocessing is presented in section 2. Sections 3 and 4 describe 2-D and 3-D, respectively, instantaneous characterization of SKR sources. As already stated, the SKR is emitted mainly on the R-X mode with possible L-O mode. We directly confirm the presence of L-O mode emission in section 5. The results are discussed in section 6.

2. Data Description

[6] The Rev 29 perikrone, with closest approach on day 2006/268 (25 September) at 2220 spacecraft event time (SCET), was selected because it allows observations out of the equatorial plane, up to ±30° latitude. The data interval analyzed covers 24 h and spans from 1000 SCET on day 2006/268 (25 September) to 1000 SCET on day 2006/269 (26 September), so that SCET values larger or smaller than 1000 SCET refer to day 2006/268 or 2006/269, respectively. The evolution of the orbital parameters during the selected period is displayed on Figures 1b, 1c, and 1d. Closest approach occurs near the local noon meridian at a distance of 4 R_S (1 R_S = 60268 km = 1 Saturn radius) from Saturn's center, when the spacecraft is at a −20° latitude (i.e., in the southern hemisphere). The equator crossing occurs after the closest approach, near 1415 LT, at 4.3 R_S. The trajectory of Cassini during this perikrone makes it particularly favorable in terms of the visibility of the radio emissions, and for the 3-D localization process (see section 4 and Appendix B).

[7] During that time the RPWS/HFR was in its so-called dipole mode (where two out of its three electrical monopole antennas are connected together and used as a dipole). We thus used only two-antenna GP inversions in this study [see *Cecconi and Zarka*, 2005]. In the two-antenna mode, we obtain four instantaneous measurements: two autocorrelation (one for each antenna) and one complex cross correlation, the real and imaginary part of which provide two independent measurements. The GP inversions consist of solving for the expressions of the six wave parameters (S, Q, U, V, θ and ϕ) as functions of the four instantaneous measurements. This implies that we have to make assumptions on at least two wave parameters. Several studied have shown that the SKR is circularly polarized: (1) although the Voyager Planetary Radio Astronomy experiment had no GP capabilities, *Ortega-Molina and Lecacheux* [1990] indirectly showed that SKR emissions observed with PRA were possibly fully circularly polarized; (2) *Cecconi et al.* [2006] reported a purely circularly polarized with a ~80% total polarization degree, using data far from Saturn, during the inbound trajectory, with the polarimeter inversion [*Cecconi and Zarka*, 2005] with an assumed source at Saturn's center; and (3) finally, *Lamy et al.* [2008b] studied 2.75 years of data and observed a fully circular polarization with high enough signal-to-noise ratio (SNR) [see *Lamy et al.*, 2008b, Figure A2]. The partial polarization reported by *Cecconi et al.* [2006] (using data with SNR of ~20 to 30 dB) is fully consistent with Figure A2 of *Lamy et al.* [2008b]. Here we use the circular goniometer inversion [*Cecconi and Zarka*, 2005; A. Lecacheux, two antenna direction finding with purely circular polarization, RPWS Team Meeting presentation, Iowa City, Iowa, 2000] for which we assume no linear polarization ($U = 0$ and $Q = 0$). Elliptically polarized SKR emission has been observed by the HFR, but only when Cassini is at latitudes >30° or <−30° (G. Fischer et al., Elliptical polarization of Saturn kilometric radiation observed from high latitudes, submitted to *Journal of Geophysical Research*, 2009). As shown by Fischer et al., the derived directions of arrival are strongly biased when observing elliptically polarized radio waves with the inversion used here. This bias can be as high as several tens of degrees and thus would be clearly visible on the data. As the selected orbit does not include spacecraft latitudes (either northern or southern) larger than 30°, our results should not be affected. The flux measurements S have been normalized to a distance of 1 astronomical unit (AU).

[8] The effective electrical antenna parameters have been calibrated during the Cassini-Jupiter flyby [*Vogl et al.*, 2004]. Calibrations have been updated with data acquired

Figure 1. (a) Dynamic spectrum of the voltage autocorrelation measured on the dipole antenna (a background value has been removed for each frequency); the red lines indicate the frequency range studied; (b) distance to Saturn in Saturn radii (R_s); (c) latitude (in degrees) in the kronian equatorial frame; (d) local time in hours; (e) polar view of the trajectory; and (f) meridian view of the trajectory. The three orbital parameters (Figures 1b, 1c, and 1d) are displayed with respect to SCET in hours of day. The vertical lines indicates the noon meridian crossing (dotted line), the equator crossing (dashed line) and the closest approach (dot-dashed line).

in early 2004, during the approach to Saturn. The analysis presented in this paper has been conducted using the updated antenna parameters, as described in Appendix A. The accuracy on effective antenna parameters (especially the effective antenna direction) is crucial for the determination of the direction of arrival of the wave. *Vogl et al.* [2004] have estimated that the accuracy on effective antenna directions is $\sim 1^\circ$.

[9] As noted by *Cecconi and Zarka* [2005], the main source of signal fluctuation on the Cassini/RPWS/HFR data is the digitization noise. Contrary to the SNR fluctuations which depend on the frequency bandwidth and on the integration time, the digitization fluctuations are proportional to the signal [*Cecconi et al.*, 2007]. In order to reduce this noise, the data have been averaged over three consecutive samples in time and three successive samples in frequency before any further processing (i.e., nine raw measurements are averaged together). The frequency band selected for this study is 13 kHz to 1.02 MHz, which is including the frequency band in which the SKR is observed ($\sim$30 kHz to $\sim$1 MHz). Considering the various sources of noise affecting the determination of the direction of arrival (SNR, galactic radio background, ambient plasma noise, receiver noise, digitization noise, geometrical configuration, inversion indetermination, calibration indetermination, intrinsic source variability, multiple sources, intrinsic size of the source) [see *Cecconi et al.*, 2007, section 2.5] and after the data preprocessing described above, the overall accuracy on the direction of arrival of the waves is $\sim 2^\circ$.

3. Goniopolarimetry: Two-Dimensional Localization

[10] The dynamic spectrum presented in Figure 1 shows the raw voltage autocorrelation measured on the dipole antenna as a function of time and frequency, for the whole RPWS/HFR frequency band. This quantity is not the radio wave flux density but the power received by the dipole antenna, which depends on its orientation with respect to the direction of the source, and also includes local plasma wave emissions and interference. In this section we present the GP results as dynamic spectra of the measured flux density, degree of circular polarization and apparent hemisphere of emission (as defined in section 3.1), as shown in Figure 2. We also provide 2-D maps of projected directions of arrival on the plane of observation, as explained in Figure 3. Figure 3 illustrates that GP inversions only retrieve the direction of arrival of incoming radio waves. An additional assumption is needed to retrieve the 3-D source location (see section 4).

3.1. Dynamic Spectra

[11] Figure 2a displays the SKR flux density normalized to 1 AU, as a function of time and frequency. As mentioned in section 2, the data have been averaged in order to reduce the digitization noise. A selection $|V| > 0.2$ has been applied in order to remove most non SKR data [*Lamy et al.*, 2008b]. Local emissions due to local plasma instabilities along the spacecraft orbit have also been removed by this selection (these emissions are visible in Figure 1a, peaking at $\sim$80 kHz at equator crossing). The narrowband emissions observed $\lesssim$50 kHz in Figure 2a have not been rejected by the selection criterion since these are also circularly polarized electromagnetic emissions. These emissions, first noticed by *Gurnett et al.* [1981], have been called n-SKR emissions (narrow band Saturn's kilometric radiation) by *Lamy et al.* [2008b]. The origin of these emissions is not understood yet. The n-SKR source characterization is beyond the scope of this study. The data selection also implies that the white areas of Figure 2a are either regions where $S < 10^{-24}$ W m^{-2} Hz^{-1}, or where $|V| < 0.2$. The selection on V allows a better definition of the SKR bursts contours as it effectively discriminates low-intensity polarized emission from unpolarized background noise. For instance, the high-frequency cutoff of SKR (at $\sim$800–1000 kHz) is better revealed by the polarization selection.

[12] Figure 2b shows the degree of circular polarization versus time and frequency. The vertical dashed line around 2220 SCET indicates the equator crossing. Before this, the SKR is mainly LH polarized, with an additional RH polarized component following the low-frequency cutoff of the LH one between 1900 SCET and the equator crossing. After equator crossing, the SKR is mainly RH polarized except for a burst of LH polarized emission below 300 kHz between 0000 and 0200 SCET.

[13] Figure 2c shows the apparent hemisphere of emission. This parameter is computed from the apparent altitude z, measured on the projection plane defined as on Figure 3. All directions of arrival with $z > 1$ (i.e., pointing to the northern hemisphere) are displayed in white, whereas the ones with $z < -1$ (i.e., pointing to the southern hemisphere) are displayed in black. Details on the 2-D projections are given in section 3.2. At this point of the analysis, we do not make any assumption on the source location. The auroral regions, within which the SKR sources are located, are in the northern or southern hemisphere. The hemisphere of emission thus provides a qualitative index for the source location. Figure 2c shows that the observed SKR is emitted mainly in that hemisphere where the spacecraft is positioned.

[14] It is clear from Figure 2 that SKR is more intense before the spacecraft crosses the equator. During this time interval, the spacecraft is in the southern morning-to-noon LT sector. Thanks to the SKR emissions temporal and spectral conjugacy observed by *Lamy et al.* [2008b], we interpret this as an enhancement of the SKR in the morning-side-to-noonside of the magnetosphere. This is known since the Voyager era [*Galopeau et al.*, 1995] and has been recently statistically studied using 2.75 years of RPWS/HFR data [*Lamy et al.*, 2008b]. We also observe emissions in both circular polarization coming from both hemispheres. The southern emissions are mainly LH circularly polarized, but with a marginal RH component, whereas northern emissions show opposite polarization characteristics. This suggests that SKR is mainly emitted on the R-X mode, but that L-O mode is also produced, even if marginally. This point is further discussed in section 5.

3.2. Two-Dimensional Source Mapping

[15] Goniopolarimetry only provides the direction of arrival of the observed radio waves. As proposed in Figure 3, it is possible to represent the observed directions of arrival as their projections on a plane perpendicular to the Cassini-Saturn line and containing the center of the planet. This plane is hereafter referred to as the projection plane. The

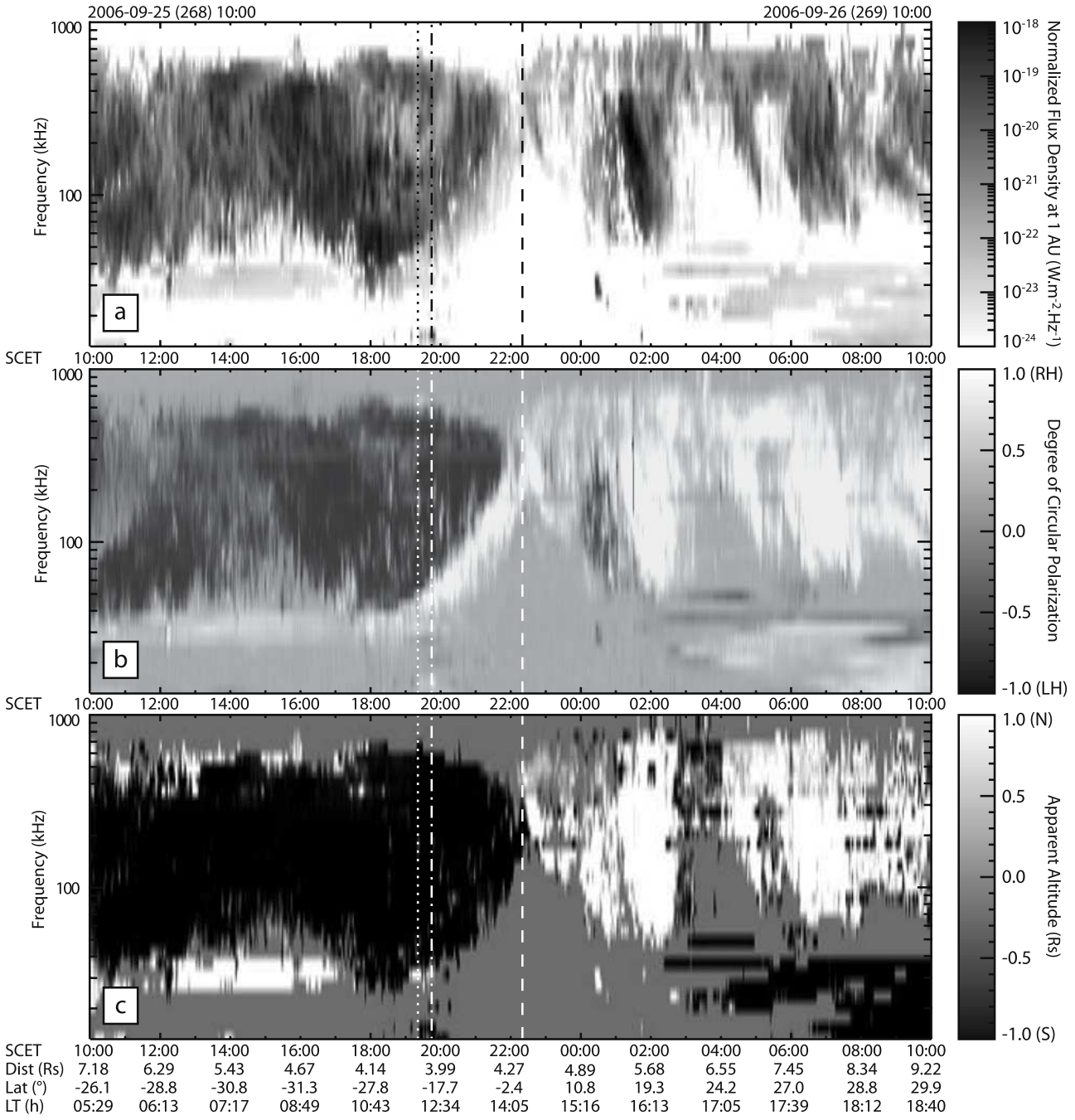

Figure 2. (a) Dynamic spectrum of the SKR flux density in W m^{-2} Hz^{-1}, (b) degree of circular polarization, and (c) apparent hemisphere of emission provided by the GP analysis. The orbital parameters are recalled at the bottom. See caption of Figure 1 for the vertical line descriptions. In Figure 2c, the apparent altitude z as defined in Figure 3 is saturated outside of the $[-1, +1]$ interval in order to display the hemisphere of emission rather than the projected altitude. For Figures 2a and 2c, the data were selected with the following condition on the circular polarization degree: $|V| > 0.2$.

projection reference frame is defined such as the x axis is along the Saturn-Cassini line, pointing to Cassini; the z axis is perpendicular to the x axis such as the north pole direction of Saturn is in the (x, z) plane; the y axis completes the orthogonal triad. The projection frame orientation changes as the spacecraft orbits Saturn. The projection plane is the (y, z) plane of the projection reference frame. In order to have consistent projection maps throughout the spacecraft orbits, the axes are scaled in R_S.

[16] Figure 4 shows four examples of projection maps built with two time intervals (day 2006/268, 1630 to 1645 SCET and day 2006/269, 0200 to 0215 SCET). Figures 4a and 4b correspond to northern hemisphere observations, and Figures 4c and 4d correspond to southern hemisphere observations. Figures 4a and 4c deal with 50–100 kHz frequency band, whereas Figures 4b and 4d show the 200–300 kHz frequency band. The contours of the $f = f_{ce}$ isosurfaces (hereinafter referred to as $\mathcal{F}_{ce}(f)$) as seen from

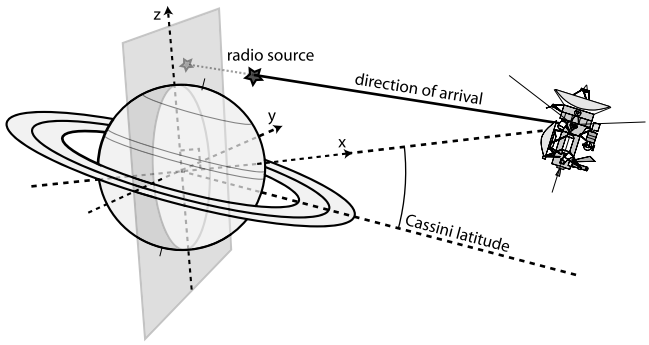

Figure 3. The goniopolarimetric inversions are providing the direction of arrival of a free-space propagating electromagnetic wave. It does not provide the actual source position. It is possible to map the source position as projection of the obtained direction of arrival on a plane (here taken as the plane perpendicular to the Cassini-Saturn line passing through the center of Saturn).

Cassini has been represented for the corresponding frequency selection bounds. The SPV magnetic field model [*Davis and Smith*, 1990], including the current sheet contribution [*Connerney et al.*, 1983] has been used to model the magnetic field and compute the $\mathcal{F}_{ce}(f)$ surfaces. These contours are also called "radio horizons" [*Farrell et al.*, 2005]. The magnetic field along the radio horizons is perpendicular to the line of sight.

[17] The CMI theory predicts at the R-X mode cutoff frequency f_X which is defined as $(f_p^2 + f_{ce}^2/4)^{1/2} + f_{ce}/2$, where f_p is the plasma frequency. As shown by *Galopeau et al.* [1989], f_X and f_{ce} are nearly identical at high latitudes. We thus use f_{ce} as the emission frequency for CMI emissions.

[18] The plotted radio horizons correspond to the upper and lower bound of the selected frequency range (the outer being the lower frequency). It is thus possible to make the four following statements that will help analyzing the maps of Figure 4: (1) any direction of arrival projected out of the outer radio horizon does not intersect its corresponding $\mathcal{F}_{ce}(f_{obs})$, where f_{obs} is the frequency of observation; (2)

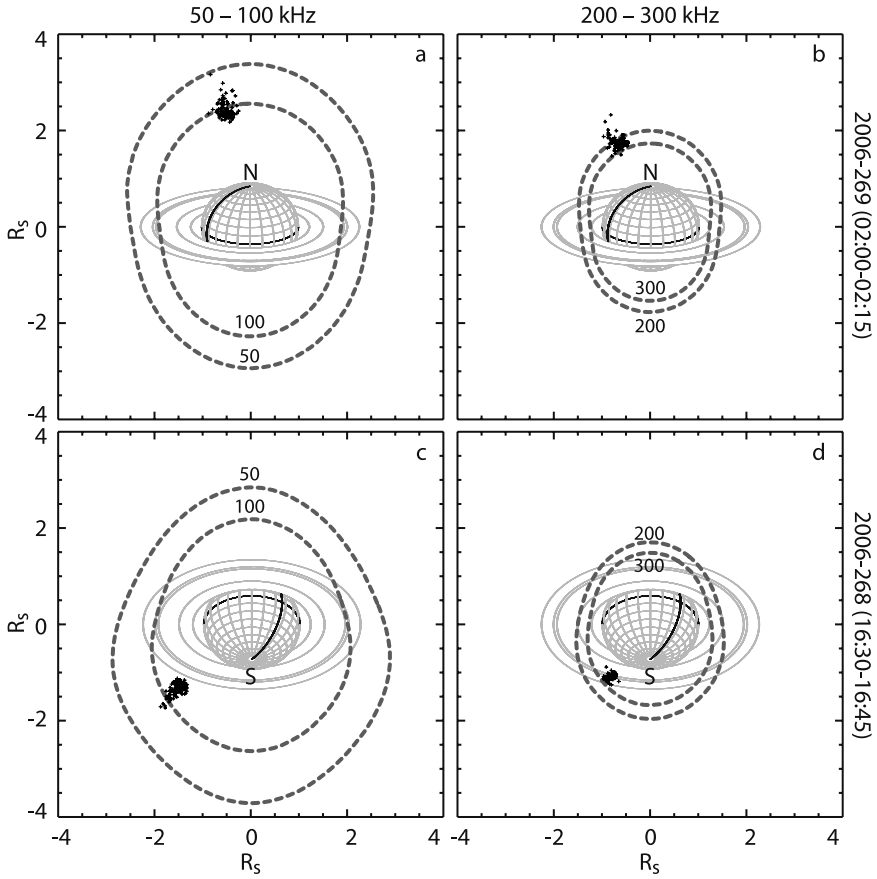

Figure 4. Two-dimensional maps projected on the *y-z* plane (see Figure 3). Data acquired in the (a and b) northern (time interval 2006/269, 0200 to 0215 SCET; distance to Saturn 5.7 R_S; latitude of the spacecraft: +21.0°; local time 1615 LT) and (c and d) southern (time interval 2006/268, 1630 to 1645 SCET; distance to Saturn 4.5 R_S; latitude of the spacecraft −36.5°; local time 0925 LT) hemispheres. Data with 50–100 kHz (Figures 4a and 4c) and 200–300 kHz (Figures 4b and 4d) frequency selection are shown. The data are also selected with a minimum SNR of 20 dB and a circular polarization degree $|V| > 0.8$. The grey dashed lines are the contour of $\mathcal{F}_{ce}(f)$ as seen from Cassini for the labeled frequency (also called "radio horizon"), as seen for the Cassini spacecraft. The noon meridian and the equator are drawn in black on Saturn.

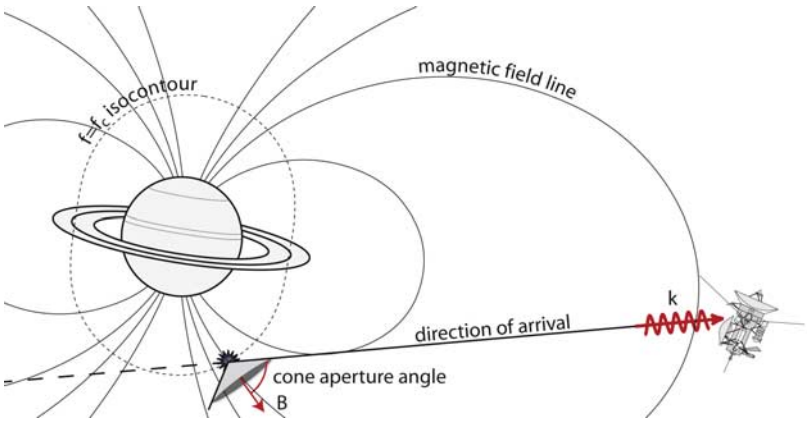

Figure 5. The goniopolarimetric inversions are providing the direction of arrival of a free-space propagating electromagnetic wave. Assuming the sources to be located in regions where the local f_{ce} is close to the observed frequency and using the planetary magnetic field model, it is possible to locate the radio sources at the intersection of the direction of arrival of the radio wave and $\mathcal{F}_{ce}(f_{obs})$. Once the source is located, the cone aperture angle of the emission and the active magnetic field line footprint location are computed.

any direction of arrival whose projection is inside the inner radio horizon necessarily intersects its corresponding $\mathcal{F}_{ce}(f_{obs})$; (3) for directions of arrival projecting between the two radio horizons, it is not possible to decide whether they intersect their respective $\mathcal{F}_{ce}(f_{obs})$ with such a map (in this case, a thorough analysis, frequency per frequency, is necessary in order to conclude); and (4) the closer the projected direction of arrival is to its respective radio horizon $\mathcal{F}_{ce}(f_{obs})$, the closer the observed beaming angle of the emission is to 90°.

[19] The projected direction of arrival on Figures 4a, 4c, and 4d are mostly within the inner radio horizon. This implies that most of the directions of arrival intersect their respective $\mathcal{F}_{ce}(f_{obs})$ and that the beaming angles of the emission are $\leq$90°. This is especially the case on Figure 4d. On Figure 4b, some projected directions of arrival are out of the outer radio horizon, and none are inside the inner radio horizon. This means that most of the data points are very close to their respective radio horizon and that the respective beaming angles are very close 90°.

[20] The overall conclusion is that the projected directions of arrival are relatively close to their respective radio horizon. Northern hemisphere observations (Figures 4a and 4b) indicate beaming angle close to 90°, at least in the highest frequency range, whereas the southern hemisphere observations (Figures 4c and 4d) indicate smaller beaming angles. The fact that some directions of arrival are observed out of the outer radio horizon (see Figure 4b) might be due to a high-latitude and high-order magnetic anomaly that is not modeled with the SPV magnetic field model that we use here.

4. Source Characterization: Three-Dimensional Localization

[21] In order to perform a 3-D localization of the SKR radio sources, we first assume that no propagation effects occur between the source and the spacecraft so that wave propagation is along a straight line. Actually, propagation effects may be important inside the sources (hereafter referred to as "close range propagation effects"), as for auroral kilometric radiation at Earth, which are produced in plasma cavities [*Calvert*, 1981; *Treumann*, 2006]. In that case, the refraction on the edge of the cavities will modify the observed beaming angle of the emission but not its position [*Mutel et al.*, 2008]. Hence, the observed beaming angle may be "real" or "apparent," depending on the existence of close range propagation effects. Only if refraction occurs further from the source (hereafter referred to as "far range propagation effects"), as described by *Xiao et al.* [2007] at Earth, then both beaming angle and source position may be strongly modified. We believe that these far range propagation effects mainly affect the lower frequencies of the SKR spectrum (below ~100 kHz) propagating at low latitudes, because of the presence of the rings' ionosphere. Taking into account such propagation effects are, however, beyond the scope of this paper, and this should be valid at high frequency and high latitude. We will hereafter call "beaming angle" the observed beaming angle, for simplicity.

[22] Assuming that the radio wave is emitted at the local f_{ce}, the source is located at the intersection of the straight line defined by the measured direction of the wave vector, and the $\mathcal{F}_{ce}(f_{obs})$ surface, as summarized on Figure 5. The detailed localization procedure and error analysis is presented in Appendix B. The same type of 3-D localization has already been applied to AKR observations [*Huff et al.*, 1988].

4.1. Active Magnetic Field Line Footprints

[23] Animation 1 shows the localization results (with both 2-D projection and active magnetic field line footprints) for the entire 24 h interval of Figure 2.[1] Each frame of Animation 1 is built from 5 min of data and is composed of two plots: a 2-D projection map on the left (with a field of view of 90° from Cassini); and a magnetic polar projection on the right. The magnetic footprints of the radio

[1] Animations are available in the HTML.

horizon (as defined in section 3.2) are represented in Animation 1 (right). They will hereinafter be referred to as "radio horizon" for simplicity. The radio horizons are displayed for each frequency range on each frame. The frequency bands and polarization are color coded as described in the caption. The directions of arrival intersecting or not $\mathcal{F}_{ce}(f_{obs})$ are represented respectively with crosses and diamonds. On the magnetic polar projections, the magnetic projection of the 2° error areas, computed as in section B2.2, have also been plotted for each direction of arrival intersecting $\mathcal{F}_{ce}(f_{obs})$.

[24] Animation 1 allows us to analyze both northern and southern sources. From 0420 to 0510 SCET and from 0555 to 0720 SCET, the RH northern sources are located between 1200 and 1600 LT, at ∼75° north magnetic latitude and emit from 100 to 400 kHz (see Figure 6, bottom). A more poleward emission is observed between 0130 and 0215 LT. The active magnetic field lines match the noon meridian and their footprints are situated at ∼80° north magnetic latitude. Finally, between 0050 and 0305 SCET, nightside sources are visible in the 400–800 kHz band (see Figure 7).

[25] For these latter data, most of the 2° error areas cover regions up to the radio horizon drawn in grey. These observations lead to the conclusion that the radio waves come from directions close to the radio horizon, indicating beaming angles close to 90°. As discussed in section B2.1, the source parameters (e.g., source localization, beaming angle) computed for sources observed close to the radio horizon are biased and cannot be readily analyzed.

[26] LH northern radio sources (possibly emitted on the L-O mode) are also observed between 0000 and 0100 SCET. They are located at ∼75° north magnetic latitude and in the 1200 to 1300 LT sector (see Figure 8 and section 5).

[27] The southern sources are more readily described when analyzing Animation 1. The LH southern radio sources are visible from 1000 to 1915 SCET. The corresponding magnetic footprints are observed from 0400 to 1400 LT, at ∼−75° southern latitude. Magnetic footprints are observed at about −68° southern latitude at ∼0800 LT. The effect of the hollow cone emission pattern of the SKR sources is clear during the whole perikrone. The magnetic footprints are indeed following or preceding the spacecraft meridian (e.g., from 1430 to 1900 SCET), as seen on Figure 6 (top). From 1700 to 1900 SCET, two active spots are visible symmetric with the spacecraft meridian, as seen on Figure 6 (middle). The localization of the magnetic footprints is thus highly dependent on the visibility of the emission. The latitudinal range in which the magnetic footprints are observed is large (from $\lesssim -70°$ to −80°). This is in the same latitudinal range in which the UV aurorae are observed. While the spacecraft is at very high southern latitudes and close enough to the planet (from 1600 to 1700 SCET), the magnetic footprints of the radio sources are clearly separated from the radio horizon, indicating a beaming angle significantly smaller than 90°.

[28] The southern source footprints are clearly separated from the radio horizon, contrary to the northern sources, indicating beaming angles smaller than in the northern hemisphere. This discrepancy between northern and southern observations is also enhanced by the fact that the spacecraft is at larger southern latitudes than in the northern case, thus providing better geometric visibility for southern observations.

[29] Finally, the equatorial shadow zone [*Lamy et al.*, 2008b] is visible at ∼2210 SCET, when the spacecraft is close the magnetic equator and below 4.3 R_S.

[30] Figure 9 summarizes the distribution of active magnetic field line footprints for the whole studied period. The footprint locations are represented with black crosses or grey diamonds, whether the corresponding direction of arrival intersects $\mathcal{F}_{ce}(f_{obs})$ or not. On Figure 9, the radio horizons are shown for the beginning and the end of the interval of observation (grey dashed lines). The intersection of all the radio horizons is the solid black line.

[31] Figure 9 (left) shows southern sources as observed by Cassini between 1000 and 2220 SCET. The southern sources are observed between ∼0200 and ∼1300 LT and between ∼−80° and −65° latitudes. At high frequency, two spots are clearly visible at 0600 LT and at 1300 LT. The oval structure is clearly visible at low frequency at ∼−70° latitude.

[32] Figure 9 (right) shows southern sources as observed by Cassini between 2220 and 1000 SCET. The northern sources are mainly observed on the noonside (from 1100 to 1600 LT), between 70° and 80° north magnetic latitude in the 100–400 kHz frequency range. A high-frequency component (400–800 kHz) is also visible on the nightside, where the distribution of the footprint locations is spread over the whole range of observable LT. In that latter frequency range, a large fraction of the directions of arrival (∼40%) are not intersecting $\mathcal{F}_{ce}(f_{obs})$. The observed footprint locations are thus likely statistically biased if the directions of arrival not intersecting $\mathcal{F}_{ce}(f_{obs})$ are not taken into account. The source parameters (e.g., source localization, beaming angle) computed for sources observed close to the radio horizon are indeed biased and cannot be readily interpreted (see section B2.1). It is likely that these emissions are coming from regions close to the radio horizon, as described by *Farrell et al.* [2005].

[33] Finally, Figure 9 also reveals that SKR sources are extending on the whole LT sector observable by Cassini during the studied interval.

4.2. Measured Beaming Angles

[34] Analyzing Figure 9 and Animation 1, we deduced that northern and southern sources do not display the same beaming properties. Figure 10 shows a statistical analysis of the beaming angle for each hemisphere (morningside of the southern hemisphere and afternoonside of the northern one) with respect of frequency. The only selection criterion used was the degree of circular polarization: $V > 0.8$ for the southern hemisphere data and $V < -0.8$ for the northern hemisphere data. This high threshold for the degree of circular polarization ensures high signal-to-noise ratio data selection, as discussed by *Lamy et al.* [2008b, Appendix A2]. No selection is made a priori on the fact that directions of arrival intersect or not their respective $\mathcal{F}_{ce}(f_{obs})$. As shown in section B2.1, excluding the directions of arrival not intersecting $\mathcal{F}_{ce}(f_{obs})$ results in biases lowering the beaming angle estimations. The two studied time intervals (2006/269, 0130 to 0730 SCET, for northern observations; 2006/268, 1300 to 1900 SCET, for southern observations) have been chosen in order to reduce the low-frequency refraction

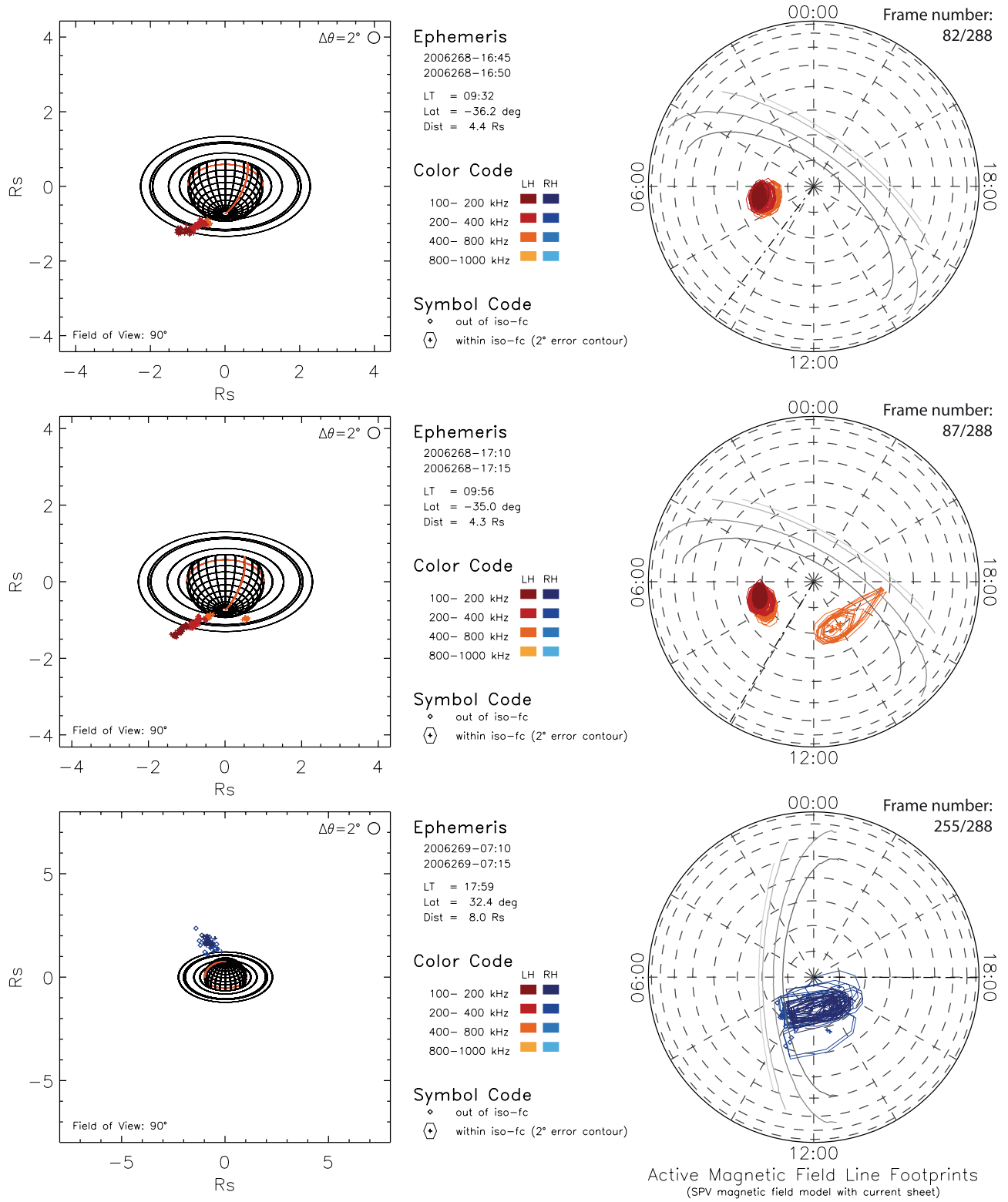

Figure 6. Still images extracted from Animation 1 showing examples of observations of SKR sources following the spacecraft meridian in the (top and middle) southern and (bottom) northern hemisphere, because of visibility effects. The frame number is given. See Animation 1 caption.

effects that could occur along the path of the radio waves when the spacecraft is too close to the equator plane.

[35] Figure 10 displays three series of data: (1) data corresponding to direction of arrival intersecting $\mathcal{F}_{ce}(f_{obs})$, in thin black lines; (2) data corresponding to direction of arrival not intersecting $\mathcal{F}_{ce}(f_{obs})$, in thin grey lines; and (3) all data, in thick black lines. For each frequency, the mean value (plain line) and the standard deviation (dashed

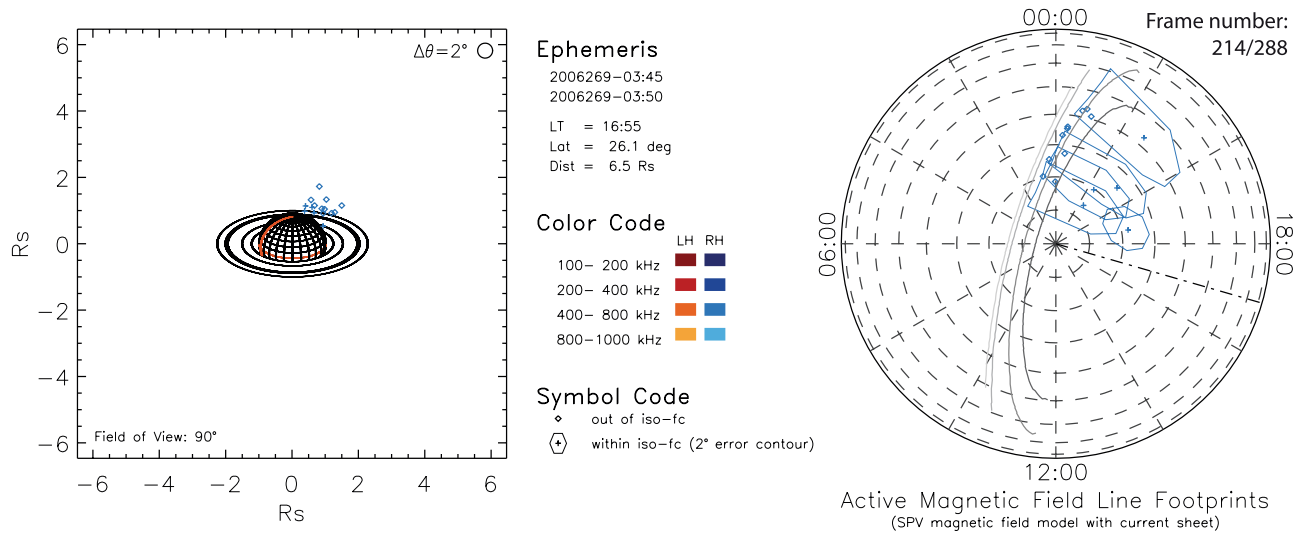

Figure 7. Still image extracted from Animation 1 showing examples of observations of SKR sources on the nightside in the northern hemisphere. The frame number is given. See Animation 1 caption.

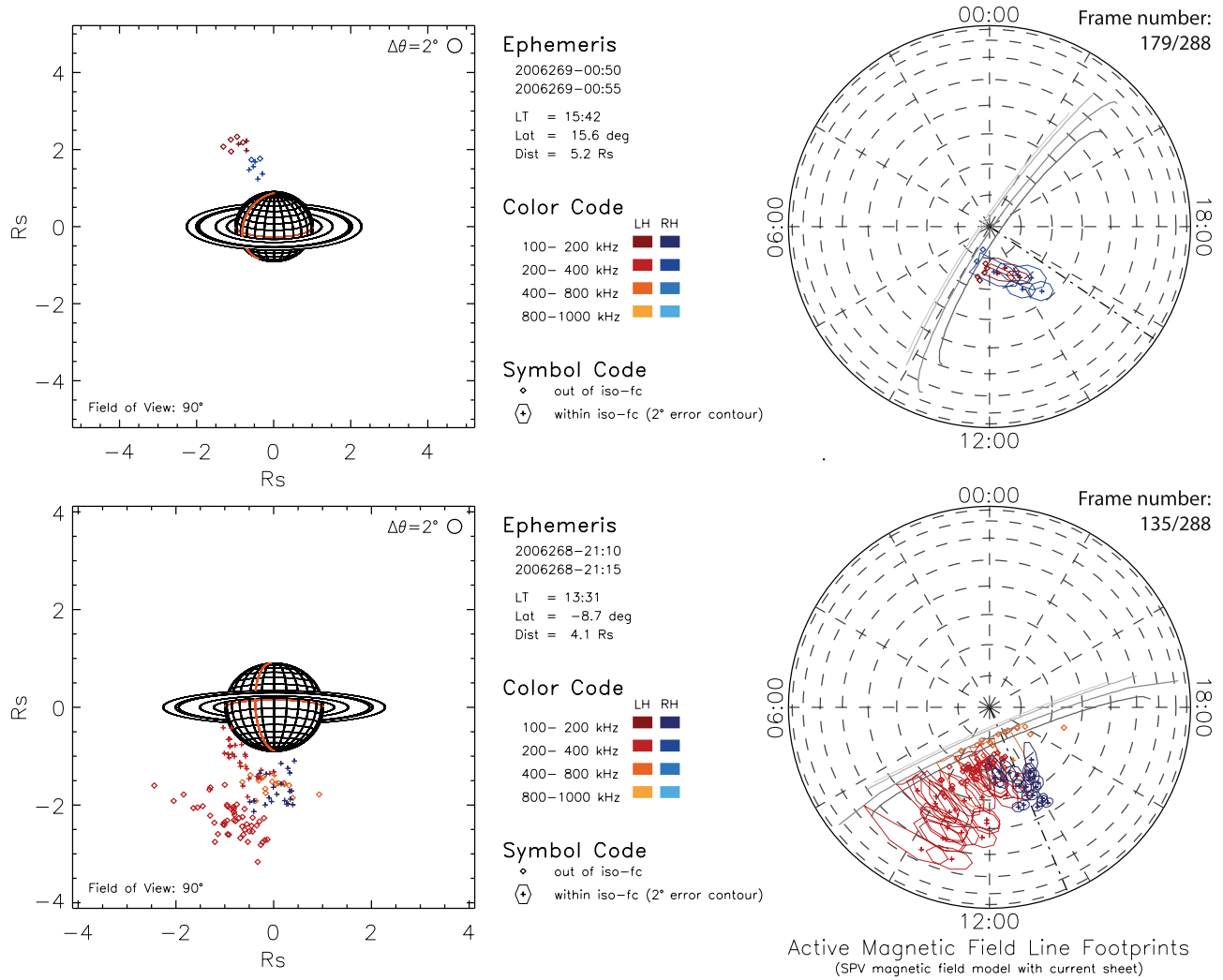

Figure 8. Still images extracted from Animation 1, showing simultaneous observation of R-X and L-O mode emissions. (top) Northern hemisphere observation, with sources on the same magnetic field line and L-O mode sources at higher altitudes than R-X sources. (bottom) Southern hemisphere observation, with L-O and R-X sources mixed in altitude.

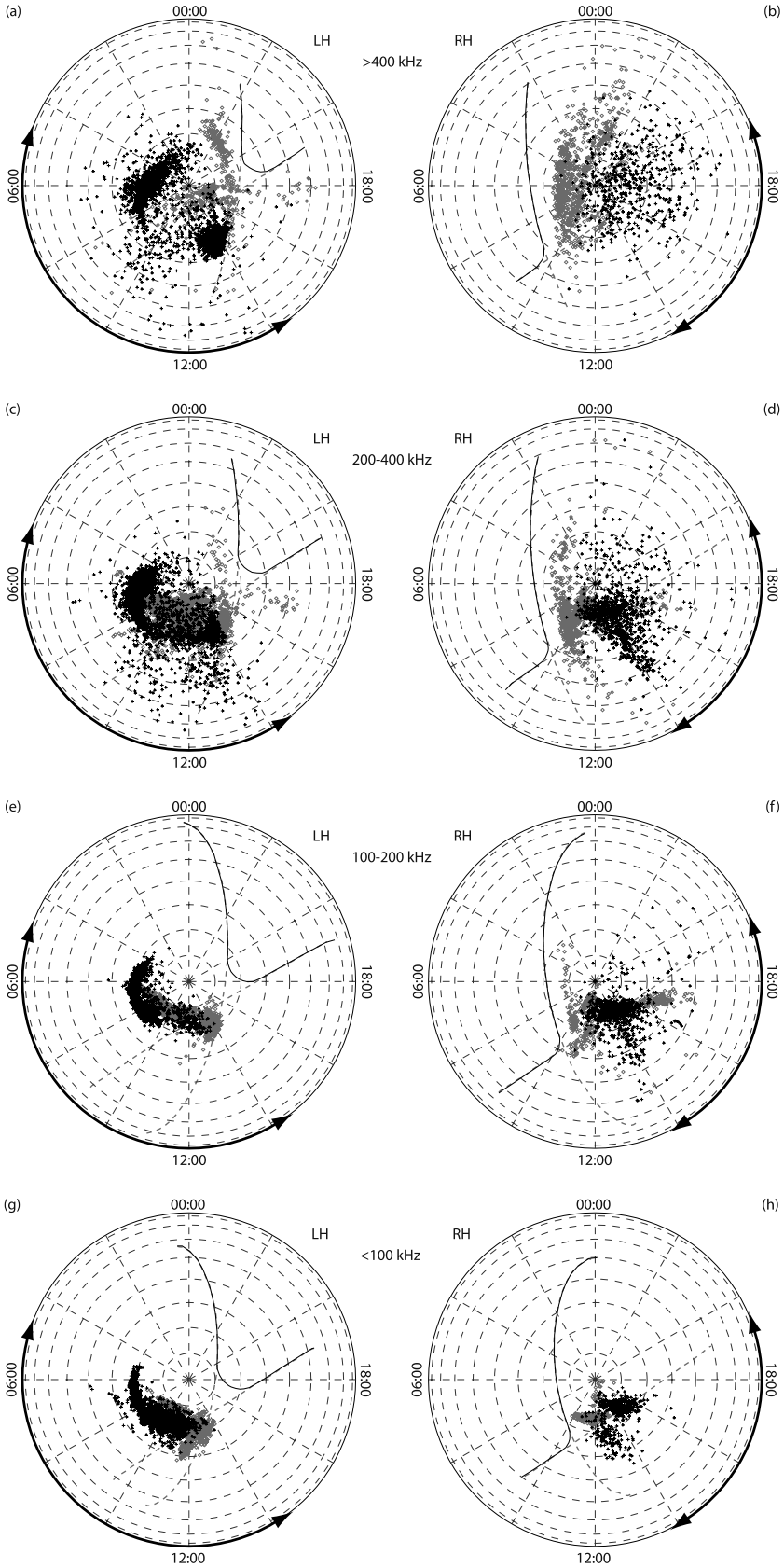
(a)
00:00
LH
>400 kHz
06:00
18:00
12:00
(b)
00:00
RH
06:00
18:00
12:00
(c)
00:00
LH
200-400 kHz
06:00
18:00
12:00
(d)
00:00
RH
06:00
18:00
12:00
(e)
00:00
LH
100-200 kHz
06:00
18:00
12:00
(f)
00:00
RH
06:00
18:00
12:00
(g)
00:00
LH
<100 kHz
06:00
18:00
12:00
(h)
00:00
RH
06:00
18:00
12:00

Figure 9

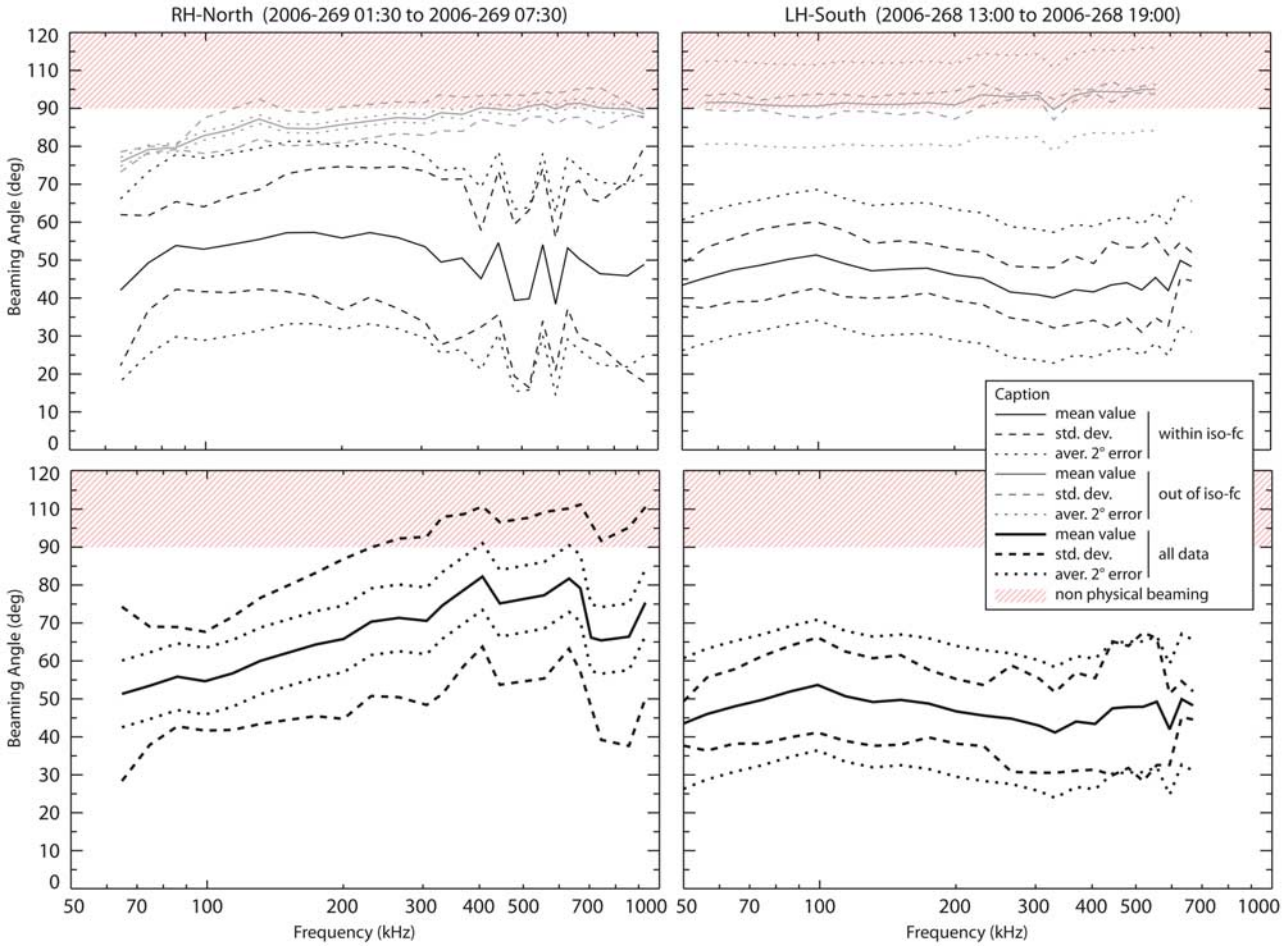

Figure 10. Beaming angle with respect to frequency (fc) for (left) northern and (right) southern sources. The data were selected with respect to circular polarization degree only: $V > 0.8$ for the southern hemisphere data and $V < -0.8$ for the northern hemisphere data. (top) The beaming angle statistics for data that intersect (in black) or not (in grey) $\mathcal{F}_{ce}$ (noted "iso-fc" in the legend). (bottom) The beaming angle statistics for all data. Displays are for 6 h of data. The average value (plain line), the corresponding standard deviation of the distribution (±1 standard deviation levels in dashed line), and the average value of the maximum simulated error adding a 2° error on each direction of arrival (dotted line) has been computed for each frequency.

lines) have been computed, taking into account only the directions of arrival intersecting $\mathcal{F}_{ce}(f_{obs})$. The corresponding standard deviation (using the same data selection) is represented in dashed lines (±1 standard deviation levels). The dotted lines represent the error on the beaming angle average value using the simulated errors discussed in section B2.2. They give maximal estimates of the error for the beaming angle determination. The beaming angle scale is extending from 0° to 120°, which seems contradictory with the fact that no beaming angles larger than 90° can be observed: a 90° beaming angle is indeed observed when the source is on the radio horizon. However, when the direction of arrival does not intersect $\mathcal{F}_{ce}(f_{obs})$, the magnetic polar projection procedure may provide source footprints beyond the radio horizon, inducing non physical beaming angles larger than 90°. The area where the beaming angle is larger than 90° has been hatched in light red.

[36] Figure 10 (left) shows the beaming angle measured between 0130 and 0730 SCET, i.e., when Cassini is in the afternoonside of the northern hemisphere. Figure 10 (bottom

Figure 9. SKR sources magnetic footprint (see Figure 5). Southern LH (Figures 9a, 9c, 9e, and 9g) and northern RH observations (Figures 9b, 9d, 9f, and 9h) are shown. The data for different frequency selections are shown: (a, b) >400 kHz, (c, d) 200–400 kHz, (e, f) 100–200 kHz, and (g, h) <100 kHz. The black crosses (and the grey diamonds are the footprints of the active magnetic field lines, whether the direction of arrival is intersecting $\mathcal{F}_{ce}$ or not, respectively. The magnetic field footprints are obtained as presented in Appendix B. The plain line gives the merged radio horizon for the whole studied period: before 2220 SCET (equator crossing) for southern data and after 2220 SCET for northern data. The radio horizons for the beginning and the end of these periods are shown in dashed grey. The LT sector in which Cassini was flying for the displayed data is highlighted by thick arrowed lines on the border of the projection maps.

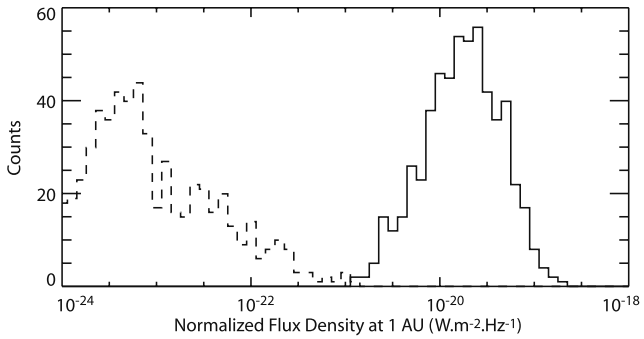

Figure 11. Flux density distributions for R-X mode (plain line) and L-O mode (dashed line). The time interval selected is 1619:12 to 1716:48 SCET for the R-X mode data and 2107:12 to 2204:48 SCET for L-O mode data. For both R-X and L-O modes, the frequency selection is 100 to 300 kHz.

left), we see that the beaming angle mean value varies from 50° to 80° in the 80–400 kHz frequency range, with uncertainties of ± ∼15°. The data samples corresponding to directions of arrival intersecting $\mathcal{F}_{ce}(f_{obs})$ (black curves on Figure 10, top left) represent 58% of the total number of data points selected for this analysis (4253 samples). The remaining 42% (grey curves on Figure 10, top left) is not negligible. The beaming angle value is thus biased by the limb effect (as discussed in section B2.1). The real beaming angle is probably somewhere in between the measured average value (i.e., ∼65° ± 15°) and 90°.

[37] Figure 10 (right) shows the beaming angle measured between 1300 and 1900 SCET, i.e., when Cassini is in the morningside of the southern hemisphere. Almost all the selected samples intersect $\mathcal{F}_{ce}(f_{obs})$ (96% of a total number of 9707 data samples). The limb effect discussed in section B2.1 is thus negligible for this data set. The average beaming angle varies with frequency: it increases from 46 ± 5° at 50 kHz, to 55 ± 7° at 100 kHz, then decreases to 50 ± 5° at 200 kHz and 45 ± 5° at 300 kHz, and finally increases again to 50 ± 10° at 500 kHz. The decreasing trend observed between 100 and 400 kHz is expected as discussed by *Lamy et al.* [2008a] (see Lamy et al.'s Figure 2, especially). The increasing trend at low frequency (below 100 kHz) can be attributed to refraction effects on the raypath. These effects have not been corrected here.

[38] For northern sources, the beaming angle estimates include 90° beaming angles, while they do not for southern sources, consistently with the discussion based on the fraction of directions of arrival intersecting or not $\mathcal{F}_{ce}(f_{obs})$.

[39] The noise on the beaming angle measurements is larger at higher frequencies, as is obvious in Figure 10. This can be easily explained by the fact that the gradient of f_{ce} steepens while going to lower altitudes: as the error on the directions of arrival is estimated to be 2°, the relative accuracy with respect to the size of $\mathcal{F}_{ce}(f_{obs})$ decreases as f_{obs} increases. This also explains why more data points do not intersect $\mathcal{F}_{ce}(f_{obs})$ in the southern hemisphere at high frequency.

[40] The northern sources thus exhibit a beaming angle closer to 90° than the southern sources. This particular point has already been theoretically discussed by *Lamy et al.* [2008a] and results from the northward shift of the magnetic equator at Saturn, implying different beaming properties in each hemisphere for the same frequencies.

5. Mode of Emission

[41] It is known from both theoretical and observational studies [*Wu*, 1985; *Benson*, 1985; *Benson et al.*, 1988] that the CMI emits radio waves mainly in the right-hand extraordinary (R-X) mode and marginally in the left-hand ordinary (L-O) mode. As the north pole of Saturn is a true magnetic north pole, the R-X mode is RH polarized in the northern hemisphere and LH in the southern one. The L-O mode is then LH in the northern hemisphere and RH in the southern one. As recalled by *Hanasz et al.* [2003], the L-O mode can be emitted either in a direct generation process when the local plasma density is sufficiently high (typically $f_{pe}/f_{ce} \gtrsim 0.3$ [*Treumann*, 2000, Figure 3]), or through partial R-X to L-O mode conversion [*Louarn and Le Quéau*, 1996]. The R-X and L-O waves have different low-frequency cutoffs, respectively, near local f_{ce} and f_{pe}.

[42] In Figures 2b and 2c, we see that an L-O emission is observed at lower frequencies than the R-X emission just before the spacecraft crosses the equator (between 1900 and 2200 SCET). The same observation occurs between 0000 and 0130 SCET, when the spacecraft is in the northern hemisphere. This has also been observed in AKR at Earth [*Roux et al.*, 1993; *Panchenko et al.*, 2008]. The L-O mode emission is observed near equator crossing, when the spacecraft is flying at the limits of the equatorial shadow zone. Two interpretations are possible: either (1) L-O mode sources have wider beaming angles than R-X ones [*Wu*, 1985; *Louarn and Le Quéau*, 1996] or (2) different refraction is sustained by L-O and R-X waves emitted from the same source but having different low-frequency cutoffs [*Xiao et al.*, 2007].

[43] We observe indeed that the flux density distribution of the R-X mode is 10^4 higher than the L-O mode flux density distribution (see Figure 11). This was also reported for AKR, using data from the Viking spacecraft [*Roux et al.*, 1993]. The ratio obtained in this paper is consistent with theoretical growth rate computations predicting L-O mode to be 10^{-3} fainter than R-X mode [*Mutel et al.*, 2007]. From that observation, it is clear that L-O mode waves are swamped in R-X mode waves if $f_{obs} > f_X$ along the raypath of the waves. That remains true for each of the two interpretations proposed in the previous paragraph.

[44] Analyzing Animation 1 can give some insights on those two interpretations. Two types of L-O mode observations can be distinguished: (1) between 2125 and 2215 SCET for the southern hemisphere and between 0000 and 0055 SCET for the northern hemisphere (see, e.g., Figure 8, top), the L-O mode emissions seem to be emitted on the same magnetic field lines as the R-X emissions, and are visible at lower frequencies (hence higher altitudes) than the R-X emissions; and (2) between 2100 and 2125 SCET, the L-O mode emissions (RH, because originating from the southern hemisphere) are coming from low altitude and are mixed with the R-X (LH) emissions (see, e.g., Figure 8, bottom). Moreover, in the latter case, L-O emissions are not located on the same magnetic field lines as R-X emissions. In case of refraction along the raypaths, it is likely that the L-O and R-X waves will not have the same direction of

arrival because of their different low frequency cutoffs. This can be interpreted as follows: direct observation of L-O mode sources, with similar or wider beaming angle than R-X mode sources, is observed in case 1, whereas refraction is occurring along the L-O mode wave raypath in case 2.

6. Discussion

[45] This study provides instantaneous SKR source characterization, including source location, beaming angle, magnetic footprint and mode of emission. The conditions of the observations were different for northern and southern sources, as Cassini observed the southern hemisphere in the dawn-to-noon LT sector, whereas the northern hemisphere was observed from early afternoon to dusk. It is, however, possible to draw similarities and differences between the sources of each hemisphere.

[46] The southern sources are observed in the 0400 to 1400 LT range, at magnetic latitudes between $-70°$ and $-80°$. The northern sources are observed on both dayside and nightside. The dayside northern sources were observed from 1200 to 1600 LT, at magnetic latitudes between 75° and 80°. Because of visibility effects, the LT range of observation is limited to 1400 LT for the upper bound of southern observation and to 1200 LT for the lower bound of northern observation. Considering this and the fact that the SKR sources ar temporally and spectrally conjugated, the dominating SKR sources are located in the 0400 to 1600 LT sector, and within 70° to 80° of absolute magnetic latitude, for both hemispheres. The LT sector that we have found here is in agreement with the statistical results obtained by *Lamy et al.* [2008b] using 2.75 years of Cassini/RPWS SKR data, as well as with those inferred through Voyager observations [*Galopeau et al.*, 1995]. Both northern and southern sources are mainly emitting on the R-X mode, and marginally on the L-O mode. We also detected nightside sources on the northern hemisphere that we could not observe in the southern hemisphere, because of visibility constraints. Nightside sources were first reported by *Farrell et al.* [2005]. That study showed that the nightside sources were observed close to the radio horizon, as found here.

[47] L-O mode emission is identified for the first time at Saturn. It displays similar characteristics as the L-O mode emission observed at Earth. From L-O sources observations, we have concluded that in some cases the L-O sources may have a wider beaming angle than the R-X ones, and in some others they may have been refracted along their raypath. The compared L-O mode and R-X mode observed phenomenology is, however, fully consistent with theoretical expectations and similar observations at Earth. Further study of many other perikrones is necessary to be able to fully characterize these emissions.

[48] We showed that the beaming angles for the morningside of the southern hemisphere and for the afternoonside of the northern one are different, possibly due to different conditions of emission as discussed by *Lamy et al.* [2008a]. Although the northern and southern absolute magnetic latitude ranges, we preferentially observe southern sources between $-68°$ and $-80°$ magnetic latitude, and northern sources between 70° and $\sim$85° magnetic latitude. This is explained by the northward shift of the magnetic dipole of Saturn. The observed beaming angles may be "real" or "apparent," dependent on the close range propagation effects (far-range propagation effects would have moved the sources away). As the CMI theory predicts a beaming angle of 90°, an observed beaming angle close to 90° indicates that we may see directly the emitting region. Lower beaming angles can be interpreted two ways: either by the presence of auroral plasma cavities, refracting the radio waves along its sides; or by a loss cone CMI emission [*Hess et al.*, 2008]. Both interpretation are consistent with the decreasing observed beaming angle with respect to frequency (as between observed 100 kHz and 400 kHz in the morningside sector of the southern hemisphere). This decrease with frequency is also consistent with simulation of the shape of the SKR arcs [*Lamy et al.*, 2008a].

[49] The source characteristics obtained here are consistent with previous studies. However, the sources LT sector and latitudinal range are biased by the visibility of the emission. This is clear in Figures 6 (top) and 6 (middle), between 1630 and 1900 SCET, where we only observe SKR sources at ±3 h of LT relative to the spacecraft position. Between 1900 and 1930 SCET (i.e., around 1200 LT), it is possible to marginally observe sources on the same LT meridian as the spacecraft (see Figure 12). These two selected examples are clearly demonstrating that the visibility changes have to be taken into account for any analysis of radio data. This implies that the general properties of the SKR sources are not provided by short time intervals ($\sim$5 min) of SKR data, but from the statistical analysis of time intervals (at least several hours) where the spacecraft is flying over a wide range of local times and/or latitudes. The interval studied in this paper meets these requirements. Thorough goniopolarimetric studies of all available perikrones are necessary to provide statistical SKR source properties. Simulation of visibility with Planetary Radio Emission Simulator (PRES) [*Hess et al.*, 2008; *Lamy et al.*, 2008a] will be of great interest to discriminate between SKR variability and visibility effects when analyzing goniopolarimetric data taken near perikrones.

[50] Magnetic latitude of SKR sources match the statistical range of observation of the UV aurora. It is also possible to map the source locations down to the equatorial plane. Using the same magnetic field model (SPV with current sheet [*Connerney et al.*, 1983]), we obtain that both northern and southern sources are mapping to an apex value of $\sim$7 R_S for the lower latitude bound and up to 20 R_S for the upper latitude bound. These L shells are computed with the current sheet model proposed by *Connerney et al.* [1983]. The use of more recent ring current modeling [e.g., *Bunce et al.*, 2007] may change these equatorial mapping of the auroral region. Moreover, *Krimigis et al.* [2007] recently showed that the plasma sheet of Saturn was highly variable and displays a strong dayside/nightside asymmetry that has to be modeled to be used for L shell studies. Systematic study of the L shell of SKR sources compared with observed electron distributions measured by the Cassini spacecraft would lead to a better understanding of the acceleration processes that produces the high-energy electrons precipitating in the auroral regions. The main difficulty of such studies lies in the following facts: when observing electron populations at high latitudes, close to the planet, it is not always possible to see the SKR source on the local magnetic field line, due to the hollow cone

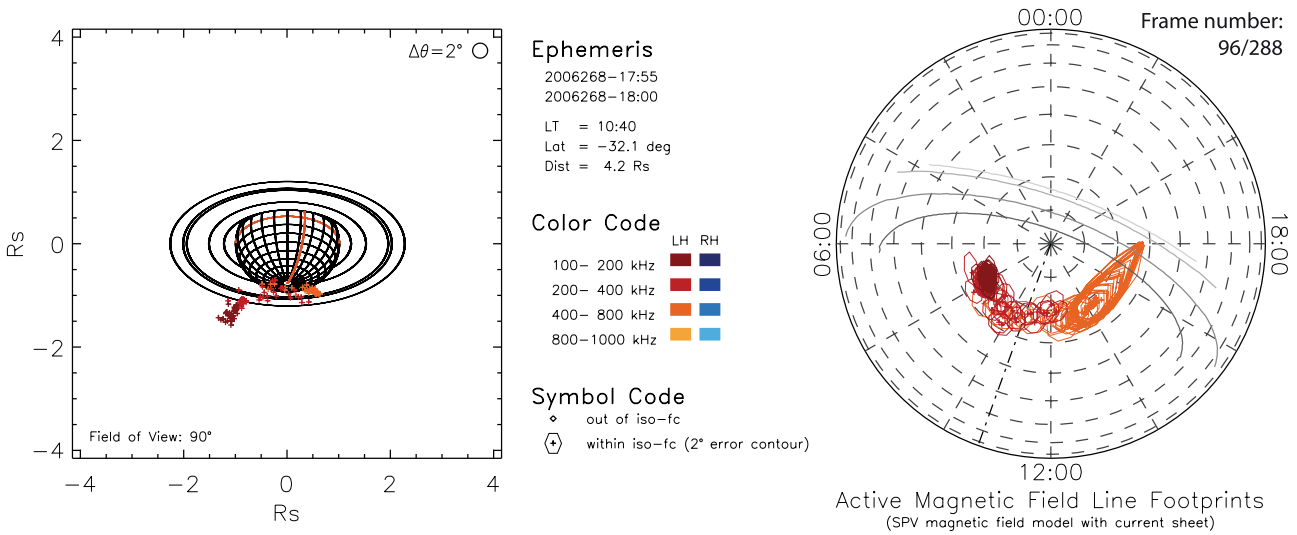

Figure 12. Still image extracted from Animation 1 showing examples of observations of SKR sources in the southern hemisphere, with sources on the spacecraft meridian. The frame number is given. See Animation 1 caption.

beaming; when observing electron at low latitudes relatively far from the planet (from 7 to 20 R_S), the accuracy on the source localization is poor, due to the fixed ∼2° error on the directions of arrival.

[51] Observing the high-frequency 2-D mapping, we concluded that a better magnetic field model close to Saturn is needed in order to get more accurate SKR source locations. Later in the mission orbits with low altitudes at high latitudes are planned; hence, huge benefits are expected for the determination of the internal kronian magnetic field and for the physics of the aurorae at Saturn.

[52] Besides the statistical study of several perikrones using the same 3-D localization techniques, perikrones where the RPWS/HFR receiver is in three-antenna mode are of particular interest. These three-antenna measurement allow us to retrieve the full polarization state of the waves, along with the directions of arrival and flux densities. Thus elliptical polarization is no more an issue. The inversion used in this study assumes circular polarization for the observed radio waves. Intrinsic elliptical polarization of the radio waves would result in a variable bias in the retrieved source position. The fact that the latitudinal range of the SKR source magnetic footprints matches that of the UV and IR aurorae, thus indicates that the observed radio waves are actually circularly polarized. Another further step of this study should include ray tracing techniques, in order to better estimate the low-frequency SKR source parameters, for which refraction is likely to occur.

7. Summary

[53] On the basis of the analysis 24 h of Cassini/RPWS/HFR data during the Rev. 29 perikrone, we have fully characterized the SKR sources. The SKR polarization is circular during the whole flyby. The SKR is mainly emitted on R-X mode, and marginally on the L-O mode. The measured beaming of the SKR sources is between ∼65° and 90° in the northern hemisphere, while it is between ∼45° and ∼60° in the southern hemisphere. The beaming angle is decreasing with frequency between 100 and 400 kHz for directions of arrivals intersecting $\mathcal{F}_{ce}(f)$. The footprints of the magnetic field lines supporting the main SKR sources are situated in the ∼70° to ∼80° northern and southern latitudinal range and in the 0400 to 1600 local time range. Northern sources are observed at slightly higher latitude (2° to 5°) than southern sources, in agreement with the northward shift of the magnetic dipole of Saturn. The location of the footprints matches that of the UV and IR aurorae. This study also reveals that the SKR sources are extending all over the range of LT that could be observed during the studied interval, with predominant sources in the morning to noon LT sector.

Appendix A: Antenna Calibration Update

[54] The Cassini/RPWS/HFR is composed of two subreceivers: the LF part covers the 3.5 to 319 kHz frequency band; the HF part scans frequencies between 325 and 16025 kHz. These two subreceivers are not using the same receiving chain. They have thus to be calibrated independently.

[55] The antenna parameters were first calibrated during the Cassini-Jupiter flyby [*Vogl et al.*, 2004], using observation in the 600 to 1350 kHz frequency band. This frequency band is exclusively scanned by the HF subreceiver of the HFR. No calibration parameter was computed for the LF subreceiver of the HFR. Moreover, during the Jupiter flyby, the HFR was operating in three antenna GP mode (measurements on three monopoles), so that no calibration has been done for the dipole mode (measurements on one dipole and one monopole). New calibrations have thus been conducted during the Cassini approach of Saturn, in the first months of 2004, using the SKR as a calibration source. On day 2004/165, Cassini is flying at ∼172 R_S from Saturn. This implies that a $3R_S$ distance at Saturn is seen with a 1° angular separation by Cassini. Hence, before this date, putting the SKR sources in the direction of Saturn implies errors on the source locations to be less than 1°. The following period of

Table A1. Relative Lengths, Colatitude, and Azimuth of the RPWS Electrical Antennas as Calibrated During the Saturn Inbound Phase[a]

	Pair of Antenna (i, w)		
	(x, w)	(u, w)	(v, w)
h_i/h_w (LF-HFR)	2.00 ± 0.16	1.08 ± 0.10	1.10 ± 0.11
h_i/h_w (HF-HFR)	2.45 ± 0.28	1.19 ± 0.09	1.22 ± 0.18
θ_i	89.3 ± 2.4	109.6 ± 4.2	111.0 ± 5.0
ϕ_i	−0.7 ± 2.5	17.2 ± 2.6	163.0 ± 3.2
θ_w	29.6 ± 4.9	28.9 ± 8.9	29.4 ± 9.7
ϕ_w	87.9 ± 5.0	89.1 ± 7.6	91.1 ± 4.9

[a]Each column corresponds to one calibration, using the (i, w) pair of antenna given in the first row, with $i = u$, v or x. The u, v, x, and w antennas are also know as $+X$, $-X$, $\pm X$ (dipole), and Z, respectively [*Cecconi and Zarka*, 2005]. The uncertainties given are the full width at half maximum of the histograms.

time has thus been selected: day 2004/152 (31 May 2004) to day 2004/165 (4 June 2004). During this time interval both three-antenna and two-antenna modes have been used, so that both modes can be calibrated.

[56] The antenna calibration inversions developed for the Jupiter flyby [*Cecconi and Zarka*, 2005] assume that the observed radio waves are purely circularly polarized. Assuming the SKR to be purely circularly polarized [*Cecconi et al.*, 2006; *Lamy et al.*, 2008b], it is possible to use it as a reference source to calibrate the effective antenna lengths and directions. The calibration results are fully described in an RPWS Team Report [*Cecconi et al.*, 2005] available upon request to corresponding author. It is also available on the RPWS/HFR-Meudon server (http://www.lesia.obspm.fr/kronos/), in the public documentation page. The results of *Cecconi et al.* [2005] are summarized in Table A1. The results of the Cassini-Jupiter encounter calibration are given in Table A2. The antenna directions obtained with the new calibration are consistent with the ones computed at Jupiter, taking into account the errors. It is, however, noticeable that we find different antenna length ratios for the LF and HF subreceivers. This discrepancy is not fully understood in terms of the receiver hardware design. The new calibration results suggest that (1) in monopole mode, the antenna directions provided by the Cassini-Jupiter calibration should be used for all frequencies; (2) in monopole mode, the antenna length ratio provided by the Cassini-Jupiter calibration should be used for data analysis above 320 kHz (HF subreceiver of the HFR); (3) in monopole mode, the antenna length ratio provided by the new calibration should be used for data analysis below 320 kHz (LF subreceiver of the HFR); and (4) in dipole mode, the new calibration set should be used for all frequencies.

[57] These results shall be used for all goniopolarimetric analysis, on any time interval. The only draw back is that the calibration was made before the Huygens Probe (HP) release, which occurred on 25 December 2004. The effective antenna parameters are supposed to be modified by the HP release. Unfortunately no calibration was done after the HP release, especially because Cassini has never been far enough from Saturn to assume the source location known with a good accuracy. The expected change on the antenna direction is of the order of $\sim 1°$ [*Vogl et al.*, 2004], which is the order of magnitude of the errors on the antenna directions. The effect of the HP release is thus not expected to have a strong influence on the effective antenna parameters.

Appendix B: Source Characterization Procedure

[58] The GP inversions provide 2-D localization characterized by two angles. In order to obtain the position of the source (i.e., the distance of the source from the spacecraft along the direction of arrival), additional hypothesis are necessary. It is known that the CMI radio emissions are emitted at the local electron cyclotron frequency f_{ce}. Using a magnetic field model, it is possible to compute the value of the magnetic field strength for each point of the line defined by the direction of arrival given by the GP inversion. As the local f_{ce} is proportional to the local magnetic field ($f_{ce} = eB/(2\pi m)$ where e and m are respectively the elementary charge and mass of the electron, and B is the local magnetic field strength), it is then possible to obtain the local f_{ce} value for each point of that line. Finding the source location is equivalent to finding the point where the local f_{ce} is equal to the frequency of observation f_{obs}.

B1. Algorithm

[59] We used the SPV magnetic field model [*Davis and Smith*, 1990], including the current sheet contribution, as modeled by *Connerney et al.* [1983]. We consider that propagation effects between the source and the observer are negligible, as Cassini is located out of the equatorial plane whereas the dense plasma regions likely to refract or scatter the radio waves are located near the equatorial plane. We assume that the radio emissions are emitted at the local f_{ce}. The source is thus at the point of intersection of the direction of arrival and the visible part of the "$f = f_{ce}$" isosurface (hereafter referred to as $\mathcal{F}_{ce}(f)$).

[60] As an initial step, the position P_0 where the local f_{ce} is the largest along the direction of arrival is computed. Comparing the value of $f_{ce}(P_0)$ to f_{obs}, we select one of the two following algorithms:

[61] 1. Algorithm $f_{ce}(P_0) \geq f_{obs}$ case means that P_0 is inside $\mathcal{F}_{ce}(f_{obs})$. We then look for the intersection of the direction of arrival and $\mathcal{F}_{ce}$ with a dichotomic algorithm. The two initial points defining the line within which the algorithm is applied are P_0 and a point P_{10} located 10 R_s toward Cassini. We proceed using the same technique as for the determination of P_0: the local f_{ce} is computed for each step of the dichotomy and after a fixed number of iterations, the position of the source P_{src} is localized with a certain accuracy. Typically, after 20 iterations, the accuracy of the computed location is less than 1 km. The accuracy on f_{ce} is then less than ~ 0.01 kHz.

[62] 2. In the algorithm $f_{ce}(P_0) < f_{obs}$ case the direction of arrival is not intersecting $\mathcal{F}_{ce}$. We search for the intersection

Table A2. Relative Length, Colatitude, and Azimuth of the RPWS Antennas as Calibrated During the Cassini-Jupiter Flyby[a]

	u Antenna	v Antenna	w Antenna
h/h_w	1.21	1.19	1.00
θ	108.3°	107.8°	29.3°
ϕ	17.0°	163.8°	90.6°

[a]See *Vogl et al.* [2004].

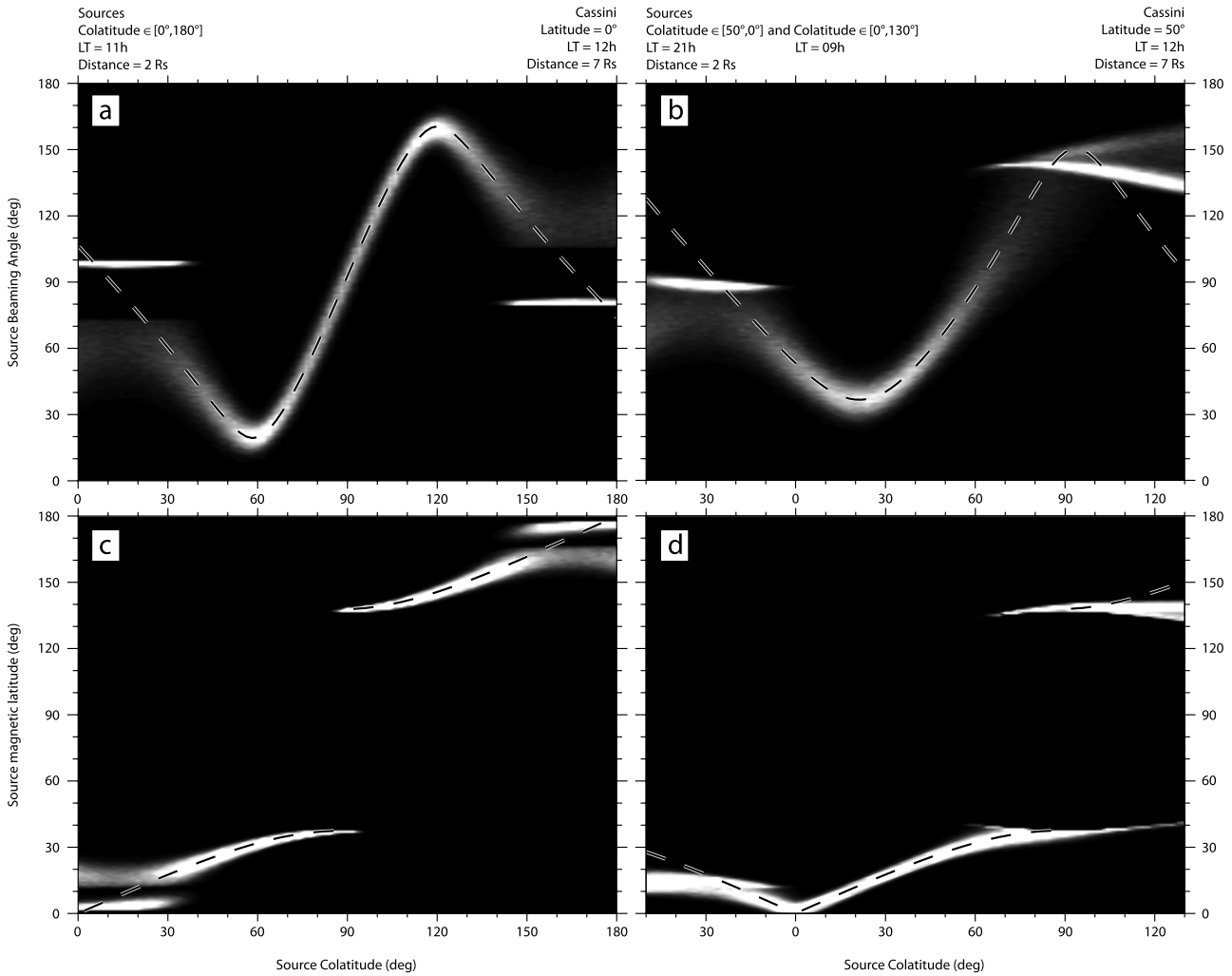

Figure B1. Error analysis on simulated data. The plots correspond to the configurations described at top. (a, b) The simulated beaming angle and (c, d) the footprint colatitude of the magnetic field on which the source is, with respect to the input source colatitude. The dashed line represents the input value of the simulated parameter. The spread of the simulated results is due to a 1° error added on the input direction of arrival.

point between $\mathcal{F}_{ce}(f_{obs})$ and the line defined by P_0 and the center of Saturn with a dichotomic algorithm. We store the obtain location P_{src} as the position of the source. We also store the distance from P_0 to P_{src}. When the direction of arrival is actually intersecting $\mathcal{F}_{ce}$ ($f_{ce}(P_0) \geq f_{obs}$ case), this distance parameter is set to zero. This distance parameter can then be used for data selection.

[63] Once the source position P_{src} is computed on $\mathcal{F}_{ce}$, the direction of the magnetic field at P_{src} provides the beaming angle of the emission θ_{src}. We also follow the magnetic field line down to the atmosphere of Saturn in order to obtain the localization of the magnetic foot print of the source P_{mfp}. The accuracy on the position of P_{mfp} is of the order of ~1°.

B2. Error Analysis

[64] The algorithm presented in Appendix B1 is using the data provided by the GP analysis. The errors on the direction of arrival determination are thus propagating into the source localization process. As described by *Cecconi and Zarka* [2005], it is possible to select the data in order to lower the uncertainties on the direction of arrival to ~1°. The selection criteria is based on both signal strength (signal-to-noise ratio) and on geometrical configuration (angular distance between the source direction and the direction of the antennas).

[65] Two error analysis have been conducted: (1) a simulation of source localization with a series of source and observer locations with several angular noise width on the simulated directions of arrival; and (2) a direct simulation of errors using real data. Both analysis are presented below.

B2.1. Simulated Sources and Observer Positions

[66] In the case of analysis 1, a series of source locations are placed along a meridian half circle at a specified local time, altitude and spanning over a 180° angular sector centered on the observer latitude. Several sets of simulation were conducted. The number of sources simulated is 91 (i.e., one simulated source every 2 degrees in geographic

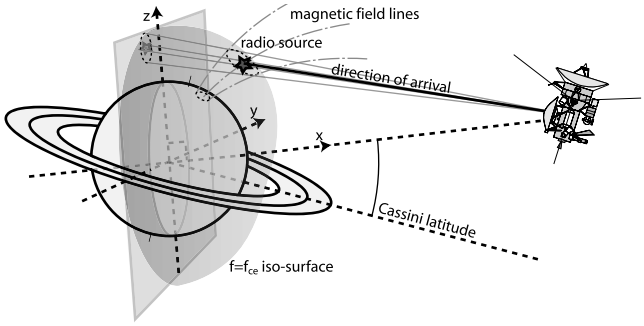

Figure B2. Simulation of errors on real data. The direction of arrival (black solid line) is given by the goniopolarimetric analysis. A series of directions of arrival is simulated on a cone (thin grey line) whose axis is the data direction of arrival. For each of the simulated direction of arrival, the source location, its beam aperture angle, and its magnetic foot print are computed.

latitude). The sources are all set at a 2 R_s distance from the center of Saturn. Such a series of sources, associated with a fixed position of the observer allows to explore the full range of possible beaming angles. As the magnetic field of Saturn is axisymmetric, the studied system has a cylindrical symmetry with respect to the north-south axis. This allows us to restrict the number of simulations as the relative local times between the source and the observer matters only. We thus choose to place the observer on the 1200 LT meridian. The sources can be either placed on local times before or after the observer's one. However, only local time meridians before the observer's one are simulated as the other half series of simulation would give the same results. The observer geographic latitude and distance to Saturn has also to be set for each simulations.

[67] The simulations have been conducted with the following set of parameters: observer latitude from 0° to 60°; observer distance to Saturn from 5 to 10 R_s; source local time from 0600 to 1200 LT. For each source the errors on the direction of arrival are simulated by adding a gaussian noise distribution (with an angular width between 1° and 10°) to the initial direction of arrival. Each resulting blurred direction of arrival distribution (5000 points are simulated each time) are used as an input to the localization routines. We then compare the distribution of the localization parameters (footprint latitude and local time, cone aperture angle, 3-D location of the source) to the initial ones.

[68] Figure B1 shows the distribution the resulting source beaming angle and the colatitude of the source magnetic field line with respect to the input one, for two simulation sets. The first column (Figures B1a and B1c) shows simulation results for an observer at 7 R_s in the equator, whereas the second one (Figures B1b and B1d) shows the case of an observer at 7 R_s in the northern hemisphere (at a latitude of +50°). The 1° error added on the simulated directions of arrival is altering localization parameters in two ways: (1) spreading the parameter distribution around the input value (see, e.g., the simulated sources between 40° and 140° in Figures B1a and B1c) and (2) adding a second biased distribution when the simulated directions are not intersecting the corresponding $\mathcal{F}_{ce}$ surface. For instance, Figure B1a is displaying such "limb effect" secondary distribution at a beaming of 95° (for sources between 0° and 40°) and at a beaming of 85° (for sources between 140° and 180°). Comparing the simulated distribution to the input parameters (dashed lines), it is clear that some the position of the observer with respect to the source is critical: the favorable observation condition being when no limb effect occurs.

B2.2. Simulated Errors on Real Data

[69] This second error analysis allows to infer direct error bars on the localization results. For each direction of arrival obtained with the goniopolarimetric inversion, a series of additional directions of arrival is build on a cone aligned with the observed direction of arrival and with an aperture angle of 2°, as described on Figure B2. The 3-D localization algorithm is applied to each series of simulated direction of arrival, giving typical error bars for each measurement of the data set. The error bars computed with this method are represented with a thin line, taking a 2° error on the directions of arrival, as seen on Figures 6 and 8.

[70] This error analysis thus provides maximal estimates of the error on the source parameters such as the source magnetic latitude, the source local time and the source beaming angle (see Figure 10).

[71] **Acknowledgments.** The research at the LESIA (Observatoire de Paris) was supported by CNES (Centre National d'Etudes Spatiales). The research at the University of Iowa was supported by NASA through contract 1279973 with the Jet Propulsion Laboratory.

[72] Wolfgang Baumjohann thanks the reviewers for their assistance in evaluating this paper.

References

Badman, S. V., S. W. H. Cowley, J.-C. Gérard, and D. Grodent (2006), A statistical analysis of the location and width of Saturn's southern auroras, *Ann. Geophys.*, *24*, 3533–3545.

Benson, R. F. (1985), Auroral kilometric radiation: Wave modes, harmonics, and source region electron density structures, *J. Geophys. Res.*, *90*, 2753–2784.

Benson, R. F., M. M. Mellott, R. L. Huff, and D. A. Gurnett (1988), Ordinary mode auroral kilometric radiation fine structure observed by DE 1, *J. Geophys. Res.*, *93*, 7515–7520.

Boischot, A., Y. Leblanc, A. Lecacheux, B. M. Pedersen, and M. L. Kaiser (1981), Arc structure in Saturn's radio dynamic spectra, *Nature*, *292*, 727–728, doi:10.1038/292727a0.

Bunce, E. J., S. W. H. Cowley, I. I. Alexeev, C. S. Arridge, M. K. Dougherty, J. D. Nichols, and C. T. Russell (2007), Cassini observations of the variation of Saturn's ring current parameters with system size, *J. Geophys. Res.*, *112*, A10202, doi:10.1029/2007JA012275.

Calvert, W. (1981), The auroral plasma cavity, *Geophys. Res. Lett.*, *8*(8), 919–921.

Cecconi, B. (2004), Étude Goniopolarimétrique des émissions radio de Jupiter et Saturne à l'aide du récepteur radio de la sonde Cassini (Goniopolarimetric study of the Jovian and Kronian radio emissions with the Cassini spacecraft radio reciever), Ph.D. thesis, Obs. de Paris-Univ. Paris 7, Meudon, France.

Cecconi, B., and P. Zarka (2005), Direction finding and antenna calibration through analytical inversion of radio measurements performed using a system of two or three electric dipole antennas on a three-axis stabilized spacecraft, *Radio Sci.*, *40*, RS3003, doi:10.1029/2004RS003070.

Cecconi, B., P. Zarka, W. S. Kurth, and D. A. Gurnett (2005), RPWS electrical antenna calibration: Saturn inbound update, technical report, Lab. d'Etudes Spatiales et d'Instrum. en Astrophys, Obs. de Paris, Paris.

Cecconi, B., P. Zarka, and W. S. Kurth (2006), SKR polarization and source localization with the Cassini/RPWS/HFR instrument: First results, in *Planetary Radio Emissions VI*, edited by H. O. Rucker, W. S. Kurth, and G. Mann, pp. 37–49, Austrian Acad. Sci. Press, Graz.

Cecconi, B., et al. (2007), STEREO/Waves goniopolarimetry, *Space Sci. Rev.*, *136*, 549–563, doi:10.1007/s11214-007-9255-6.

Connerney, J. E. P., M. H. Acuña, and N. F. Ness (1983), Currents in Saturn's Magnetosphere, *J. Geophys. Res.*, *88*, 8779–8789.
Cowley, S. W. H., E. J. Bunce, and R. Prangé (2004), Saturn's polar ionospheric flows and their relation to the main auroral oval, *Ann. Geophys.*, *22*, 1379–1394.
Davis, L. J., and E. J. Smith (1990), A model of Saturn's magnetic field based on all available data, *J. Geophys. Res.*, *95*, 15,257–15,261.
Ergun, R. E., et al. (1998), FAST satellite wave observations in the AKR source region, *Geophys. Res. Lett.*, *25*, 2061–2064.
Ergun, R. E., C. W. Carlson, J. P. McFadden, G. T. Delory, R. J. Strangeway, and P. L. Pritchett (2000), Electron-cyclotron maser driven by charged-particle acceleration from magnetic field-aligned electric fields, *Astrophys. J.*, *538*, 456–466.
Farrell, W. M., M. D. Desch, M. L. Kaiser, A. Lecacheux, W. S. Kurth, D. A. Gurnett, B. Cecconi, and P. Zarka (2005), A nightside source of Saturn's kilometric radiation: Evidence for an inner magnetosphere energy driver, *Geophys. Res. Lett.*, *32*, L18107, doi:10.1029/2005GL023449.
Galopeau, P., P. Zarka, and D. Le Quéau (1989), Theoretical model of Saturn's kilometric radiation spectrum, *J. Geophys. Res.*, *94*, 8739–8755.
Galopeau, P. H. M., P. Zarka, and D. Le Quéau (1995), Source location of Saturn's kilometric radiation: The Kelvin-Helmholtz instability hypothesis, *J. Geophys. Res.*, *100*, 26,397–26,410.
Gérard, J. C., V. Dols, D. Grodent, J. H. Waite, G. R. Gladstone, and R. Prangé (1995), Simultaneous observations of the saturnian aurora and polar haze with the HST/FOC, *Geophys. Res. Lett.*, *22*, 2685–2688.
Gérard, J.-C., D. Grodent, J. Gustin, A. Saglam, J. T. Clarke, and J. T. Trauger (2004), Characteristics of Saturn's FUV aurora observed with the Space Telescope Imaging Spectrograph, *J. Geophys. Res.*, *109*, A09207, doi:10.1029/2004JA010513.
Gurnett, D. A., W. S. Kurth, and F. L. Scarf (1981), Narrowband electromagnetic emissions from Saturn's magnetosphere, *Nature*, *292*, 733–737, doi:10.1038/292733a0.
Gurnett, D. A., et al. (2004), The Cassini radio and Plasma wave science investigation, *Space Sci. Rev.*, *114*(1–4), 395–463.
Hanasz, J., M. Panchenko, H. de Feraudy, R. Schreiber, and M. M. Mogilevsky (2003), Occurrence distributions of the auroral kilometric radiation ordinary and extraordinary wave modes, *J. Geophys. Res.*, *108*(A11), 1408, doi:10.1029/2002JA009579.
Hess, S., B. Cecconi, and P. Zarka (2008), Modeling of Io-Jupiter decameter arcs, emission beaming and energy source, *Geophys. Res. Lett.*, *35*, L13107, doi:10.1029/2008GL033656.
Huff, R. L., W. Calvert, J. D. Craven, L. A. Frank, and D. A. Gurnett (1988), Mapping of auroral kilometric radiation sources to the aurora, *J. Geophys. Res.*, *93*, 11,445–11,454.
Kaiser, M. L., M. D. Desch, J. W. Warwick, and J. B. Pearce (1980), Voyager detection of nonthermal radio emission from Saturn, *Science*, *209*, 1238–1240.
Kaiser, M. L., M. D. Desch, W. S. Kurth, A. Lecacheux, F. Genova, B. M. Pedersen, and D. R. Evans (1984), Saturn as a radio source, in *Saturn*, pp. 378–415, Univ. of Ariz. Press, Tucson.
Krimigis, S. M., N. Sergis, D. G. Mitchell, D. C. Hamilton, and N. Krupp (2007), A dynamic, rotating ring current around Saturn, *Nature*, *450*, 1050–1053, doi:10.1038/nature06425.
Kurth, W. S., et al. (2005), An Earth-like correspondence between Saturn's auroral features and radio emission, *Nature*, *433*, 722–725.
Lamy, L., P. Zarka, B. Cecconi, S. Hess, and R. Prangé (2008a), Modeling of Saturn kilometric radiation arcs and equatorial shadow zone, *J. Geophys. Res.*, *113*, A10213, doi:10.1029/2008JA013464.
Lamy, L., P. Zarka, B. Cecconi, R. Prang, W. S. Kurth, and D. A. Gurnett (2008b), Saturn kilometric radiation: Average and statistical properties, *J. Geophys. Res.*, *113*, A07201, doi:10.1029/2007JA012900.
Louarn, P. (1992), Auroral planetary radio emissions: theoritical aspects, *Adv. Space. Res.*, *12*(8), 121–134.
Louarn, P., and D. Le Quéau (1996), Generation of the auroral kilometric radiation in plasma cavities—II. The cyclotron maser instability in small size sources, *Planet. Space Sci.*, *44*(3), 211–224.
Mutel, R. L., W. M. Peterson, T. R. Jaeger, and J. D. Scudder (2007), Dependence of cyclotron maser instability growth rates on electron velocity distributions and perturbation by solitary waves, *J. Geophys. Res.*, *112*, A07211, doi:10.1029/2007JA012442.
Mutel, R. L., I. W. Christopher, and J. S. Pickett (2008), Cluster multi-spacecraft determination of AKR angular beaming, *Geophys. Res. Lett.*, *35*, L07104, doi:10.1029/2008GL033377.
Ortega-Molina, A., and A. Lecacheux (1990), Polarization response of the Voyager-PRA experiment at low frequencies, *Astron. Astrophys.*, *229*, 558–568.
Panchenko, M., J. Hanasz, and H. O. Rucker (2008), Estimation of linear wave polarization of the auroral kilometric radiation, *Radio Sci.*, *43*, RS1006, doi:10.1029/2006RS003606.
Queinnec, J., and P. Zarka (1998), Io-controlled decameter arcs and Io-Jupiter interaction, *J. Geophys. Res.*, *103*, 26,649–26,666.
Roux, A., A. Hilgers, H. de Feraudy, D. le Queau, P. Louarn, S. Perraut, A. Bahnsen, M. Jespersen, E. Ungstrup, and M. Andre (1993), Auroral kilometric radiation sources: In situ and remote observations from Viking, *J. Geophys. Res.*, *98*, 11,657–11,670.
Stallard, T. S., S. Miller, H. Melin, M. Lystrup, S. W. H. Cowley, E. J. Bunce, N. Achilleos, and M. K. Dougherty (2008a), Jovian-like aurorae on Saturn, *Nature*, *453*, 1083–1085, doi:10.1038/nature07077.
Stallard, T. S., et al. (2008b), Complex structure within Saturn's infrared aurora, *Nature*, *456*, 214–217, doi:10.1038/nature07440.
Trauger, J. T., et al. (1998), Saturn's hydrogen aurora: Wide field and planetary camera 2 imaging from the Hubble Space Telescope, *J. Geophys. Res.*, *103*(12), 20,237–20,244.
Treumann, R. A. (2000), Planetary radio emission mechanisms: A tutorial, in *Radio Astronomy at Long Wavelengths*, *Geophys. Monogr. Ser.*, vol. 119, edited by R. G. Stone et al., pp. 329–337, AGU, Washington, D. C.
Treumann, R. A. (2006), The electron-cyclotron maser for astrophysical application, *Astron. Astrophys. Rev.*, *13*, 229–315, doi:10.1107/s00159-006-0001-y.
Vogl, D. F., et al. (2004), In-flight calibration of the Cassini-Radio and Plasma Wave Science (RPWS) antenna system for direction-finding and polarization measurements, *J. Geophys. Res.*, *109*, A09S17, doi:10.1029/2003JA010261.
Wu, C. S., and L. C. Lee (1979), A theory of the terrestrial kilometric radiation, *Astrophys. J.*, *230*, 621–626.
Wu, C.-W. (1985), cyclotron and synchroton Maser instabilities: Radio emission processes by direct amplification of radiation, *Space Sci. Rev.*, *41*, 215–298.
Xiao, F., L. Chen, H. Zheng, and S. Wang (2007), A parametric ray tracing study of superluminous auroral kilometric radiation wave modes, *J. Geophys. Res.*, *112*, A10214, doi:10.1029/2006JA012178.
Zarka, P. (1998), Auroral radio emissions at the outer planets: Observations and theories, *J. Geophys. Res.*, *103*, 20,159–20,194.
Zarka, P. (2000), Radio emissions from the planets and their moons, in *Radio Astronomy at Long Wavelengths*, *Geophys. Monogr. Ser.*, vol. 119, edited by R. G. Stone et al., pp. 167–178, AGU, Washington, D. C.

B. Cecconi (corresponding author), L. Lamy, R. Prangé, and P. Zarka, LESIA, Observatoire de Paris, 5 Place Jules Janssen, F-92190 Meudon, France. (baptiste.cecconi@obspm.fr)

W. S. Kurth, Department of Physics and Astronomy, University of Iowa, Iowa City, IA 52242-1479, USA.

P. Louarn, Centre d'Etude Spatiale des Rayonnements, Université Paul Saltier, CNRS, 9 avenue Colonel Roche, F-31329 Toulouse, France.